

Willman 1 Revisited: The Kinematics, Chemistry, and Orbital Properties of a Potentially-Disrupting Dwarf Galaxy

CAMILLE CHIU ,¹ MARLA GEHA ,¹ WILLIAM CERNY ,¹ NITYA KALLIVAYALIL ,² HANNAH RICHSTEIN ,² CHRISTOPHER T. GARLING ,² AND BETH WILLMAN ,³

¹Department of Astronomy, Yale University, New Haven, CT 06520, USA

²Department of Astronomy, University of Virginia, Charlottesville, VA 22904, USA

³LSST Discovery Alliance, 933 North Cherry Avenue, Tucson, AZ 85719, USA

ABSTRACT

The ultra-faint Milky Way satellite Willman 1 (W1; $M_V = -2.6$; $r_{\text{half}} \sim 27$ pc) was the first stellar over-density found via resolved stars in the Sloan Digital Sky Survey, yet its classification as a dwarf galaxy or star cluster remains ambiguous. Using new Keck/DEIMOS spectroscopy, *HST/ACS* photometry, and orbital modeling, we re-examine the nature of W1. From our updated member sample of 57 stars, we find that past analyses included four binaries and seven non-members, identified using *Gaia* proper motions and updated velocities. We continue to find a velocity dispersion consistent with previous analyses, measuring $\sigma_v = 4.7^{+1.5}_{-1.3}$ km s⁻¹ from 49 stars out to $3r_{\text{half}}$. If W1 is in equilibrium, this suggests a dynamical mass of $5.9^{+3.7}_{-3.4} \times 10^5 M_\odot$ and mass-to-light ratio of $(M/L)_V = 660 \pm 590$. Based on Ca II triplet measurements, we estimate an iron abundance of $[\text{Fe}/\text{H}] = -2.45^{+0.12}_{-0.13}$ and metallicity dispersion of $\sigma_{[\text{Fe}/\text{H}]} = 0.30^{+0.15}_{-0.11}$ dex. We confirm that W1 does not exhibit mass segregation inside $\sim 1 r_{\text{half}}$. Our best-fit orbital model predicts that W1 is at apocenter, implying that W1 has been closer to the Milky Way in the recent past with a pericentric passage $\lesssim 25$ kpc from the Galactic center ~ 0.3 Gyr ago. Given its internal kinematics, metallicity spread, and lack of mass segregation, we conclude that W1 is a galaxy. However, given its orbit and structural properties, which suggest that W1 might be tidally disrupted, as well as the difficulty in identifying a pure member sample, we caution that the measured internal velocity dispersion may not accurately reflect the dynamical mass of this system.

Keywords: Dwarf galaxies — Stellar kinematics — Milky Way dynamics

1. INTRODUCTION

The advent of wide-field photometric surveys such as the Sloan Digital Sky Survey (SDSS) and the Dark Energy Survey (DES) has led to the rapid discovery of several dozen Milky Way satellite galaxies, including populations of ultra-faint dwarf galaxies and ultra-faint star clusters (e.g., Willman et al. 2005; Belokurov et al. 2007; Drlica-Wagner et al. 2015; Koposov et al. 2015; Torrealba et al. 2016; Homma et al. 2024; Cerny et al. 2024). The faintest and most compact of these stellar systems, with stellar masses of only a few hundred solar masses and half-light radii of only tens of parsecs, blur the line between globular clusters and dwarf galaxies (e.g., Smith et al. 2024). The classification of an object as a dwarf galaxy or star cluster typically hinges on one or both of the following diagnostics (Willman & Strader 2012): (1) a kinematic distribution that cannot be explained solely by its baryonic component, implying the presence of large quantities of dark matter; (2) a spectroscopically observed spread in $[\text{Fe}/\text{H}]$ metallicity, indicating multiple epochs of star formation. Beyond these two criteria, the presence of mass segre-

gation has also been proposed as a discriminator (Baumgardt et al. 2022).

One such system that straddles the boundary between dwarf galaxies and globular clusters is the Milky Way satellite Willman 1 (W1; SDSSJ1049+5103). W1 was first identified as an over-density of old, metal-poor stars in SDSS DR2 by Willman et al. (2005) and was the lowest luminosity galaxy known at the time of discovery ($M_V = -2.5$; Willman et al. 2005). Despite tentative evidence for mass segregation, Willman et al. (2006) initially leaned towards a dwarf galaxy classification for W1 based on an observed metallicity spread between three red giant branch (RGB) stars. This classification was supported by Keck/DEIMOS spectroscopy by Martin et al. (2007), who identified seven RGB members with a significant metallicity spread. However, follow-up spectroscopy from the Hobby-Eberly Telescope by Siegel et al. (2008) determined that at least two and up to five of these identified RGB stars were likely Milky Way foreground dwarf stars, significantly decreasing the observed metallicity spread. From a reanalysis with Keck/DEIMOS spectroscopy and a careful characterization of foreground con-

tamination, Willman et al. (2011) identified 45 member stars, 40 of which were classified as high confidence. This included an additional RGB member and two horizontal branch members whose metallicity spread was once again indicative of a dwarf galaxy. These spectroscopic results are confirmed by the photometric *HST*-based metallicity distribution function measured by Fu et al. (2023), who determined a significant metallicity spread of $\sigma_{[\text{Fe}/\text{H}]} = 0.65^{+0.10}_{-0.09}$ dex.

Assuming equilibrium, Willman et al. (2011) estimated the dynamical mass of W1 to be $\sim 3.9 \times 10^5 M_\odot$ based on a velocity dispersion of $4.8 \pm 0.8 \text{ km s}^{-1}$, implying a mass-to-light (M/L) ratio of ~ 770 . Due to this apparent high dark matter content and relatively close proximity at a distance of ~ 38 kpc, W1 remains one of the most promising targets in the search for dark matter annihilation signals in gamma rays (e.g., Aliu et al. 2009; Bringmann et al. 2009; Li et al. 2021; McDaniel et al. 2023) and X-rays (e.g., Nieto & Mirabal 2010; Loewenstein & Kusenko 2010, 2012; Saeedi & Sasaki 2020).

Yet, previous studies of W1 found evidence for dynamical disequilibrium, including stellar multi-directional tails and a tentative excess of stars at large half-light radii (Willman et al. 2006, 2011). Specifically, Willman et al. (2011) reported an irregular kinematic distribution where stars within the effective half-light radius have a systematically higher velocity than those beyond; this disturbed morphology might point to tidal interactions. If W1 is not in dynamical equilibrium and indeed is undergoing tidal disruption, then the dynamical mass inferred from its internal velocity dispersion may be misleading.

The main difficulty in accurately classifying W1 and determining its properties lies in the kinematic and spectroscopic similarities between the foreground stars in the Milky Way and the members of W1 (Siegel et al. 2008; Willman et al. 2011; Saeedi & Sasaki 2020). With an estimated systemic radial velocity of $-12.8 \pm 1.0 \text{ km s}^{-1}$, the velocities of W1 stars substantially overlap with the velocities of Milky Way stars (Willman et al. 2011). If W1 is dynamically disturbed, spatial and kinematic cuts, which are often implemented to supplement photometric color-magnitude diagram (CMD) cuts, might instead obscure the odd structural and kinematic features of W1. On the other hand, due to the already small sample size of stars, just a few Milky Way contaminants in the member sample could artificially alter the velocity dispersion, and thus the inferred dynamical mass of W1, as well as the metallicity spread that is used to characterize it as a dwarf galaxy in the first place.

To address these uncertainties, this paper revisits W1 and presents a comprehensive study of its structural, kinematic, chemical, and orbital properties. First, we describe our uniform analysis of both new and archival Keck/DEIMOS spectroscopy for W1 and our incorporation of *Gaia* astrometry

(§2). We then discuss the probabilistic membership selection performed to reduce the presence of Milky Way foreground contamination (§3). From this member sample, we measure the properties of W1 including its velocity dispersion, inferred dynamical mass, and metallicity distribution (§4). With *HST/ACS* imaging of W1, we summarize previous results for W1’s star formation history and look for evidence of mass segregation (§5). We next model the orbital history of W1 and simulate mock tidal streams (§6). We conclude with a discussion of W1’s classification as either a dwarf galaxy or star cluster and its tidal disruption status (§7).

2. OBSERVATIONS AND DATA REDUCTION

Our kinematic and metallicity analysis is based on a homogeneous reduction of archival Keck/DEIMOS spectroscopic data (§2.1, §2.2), half of which are published here for the first time. We supplement this with ground-based photometry and *Gaia* astrometry (§2.3).

2.1. Keck/DEIMOS Spectroscopy: Kinematics

We present homogeneously reduced archival data of W1 from the DEIMOS spectrograph (Faber et al. 2003) on the Keck II 10-m telescope. Twelve multislit masks were taken of W1 between 2006–2023 (see Table 1). One of these masks was first presented in Martin et al. (PI: Chapman 2007) and four masks were published in Willman et al. (PI: Brodie 2011). The remaining seven masks are presented here for the first time [PIs: Geha, Rich]. All data were taken with the 1200G grating, providing a spectral resolving power of $R \sim 6000$ at 8500 \AA . The spectral dispersion of this setup is roughly 0.33 \AA per pixel with a resulting spectral resolution of 1.37 \AA (FWHM). A summary of observations is presented in Table 1.

A detailed discussion of the data reduction is presented in Geha et al. (2026) and briefly discussed here. Raw science frames and associated calibrations were obtained through the Keck Observatory Archive⁴. Data were reduced to one dimensional wavelength-calibrated spectra using the open-source python-based data reduction code PypeIt (Prochaska et al. 2020). PypeIt reduces the eight individual DEIMOS detectors as four mosaic images, where each red/blue pair of detectors is reduced together.

Stellar radial velocities were measured using the dmost package (Geha et al. 2026)⁵. dmost first pre-processes spectra to identify and remove extragalactic objects using a modified version of the automated redshift software Marz (Hinton et al. 2016). For the remaining spectra, dmost forward models the 1D spectrum for each source from a given exposure with both a stellar template from the PHOENIX li-

⁴ <https://koa.ipac.caltech.edu>

⁵ <https://github.com/marlageha/dmost>

brary (Husser et al. 2013) and a synthetic telluric absorption spectrum from TelFit (Gullikson et al. 2014). The velocity is determined for each science exposure through an MCMC procedure constraining both the radial velocity of the target star as well as a wavelength shift of the telluric spectrum needed to correct for slit miscentering (see, e.g., Sohn et al. 2007). We reject velocities where the posterior shape is far from Gaussian, largely spectra with $S/N < 3$. The final radial velocity for each star is derived through an inverse-variance weighted average of the velocity measurements from each individual exposure. In cases where less than half of individual science exposures for a given star produce a reliable velocity measurement, we attempt to measure a velocity based on the 1D coadded spectrum following the same method above. In both cases, a velocity error scaling and velocity floor is applied to the random errors, based on an assessment from thousands of repeat DEIMOS measurements as discussed in Geha et al. (2026). The velocity error floor is 1.1 km s^{-1} for a velocity measured on a single mask.

There are 474 unique targets with extracted DEIMOS spectra, plus 28 sources extracted serendipitously in addition to the target source. We have photometry and were able to measure radial velocities for 340 of these sources. 125 of these sources are extragalactic, including 14 broad-line quasar spectra. The remaining 215 sources have velocities and spectra consistent with stars, although we expect only a fraction of these to be W1 members (see §3.1). 12 of these sources have velocity uncertainties greater than 15 km s^{-1} , above the threshold considered as a secure velocity measurement by Geha et al. (2026), and are thus not considered for membership. We therefore consider 203 stars with measured radial velocities for membership. The radial velocities for the 203 stars and redshifts for the 125 extragalactic sources are available in Table A3 and A4 of Geha et al. (2026), respectively.

2.1.1. Flagging Velocity Variables

The orbital motions of unresolved binary stars systems when measured at a single epoch can inflate a system’s inferred velocity dispersion. To identify such velocity variable stars, we evaluate whether velocities measured at different times are consistent with random fluctuations from a constant value. For each star, we first calculate the weighted mean velocity, the equivalent of assuming a constant velocity model. We then calculate the χ^2 value for this model, including random and systematic error components. Following Maxted et al. (2001), we then calculate the probability, p , of obtaining the observed value of χ^2 or higher from random fluctuations around a constant value. p is evaluated for the appropriate number of degrees of freedom (the number of observations minus one). We define a star as a velocity variable if $\log_{10} p < -1$. 63 out of 340 stars have velocities

measured on multiple DEIMOS mask pointings, all of which have measurements separated by more than one year. We find 16 of these stars to be velocity variables, 6 of which are members. Their positions on the CMD are shown in Figure 1a.

2.2. Keck/DEIMOS Spectroscopy: Metallicities

We use dmost to measure the equivalent width of several stellar absorption lines. We first determine equivalent widths for NaI: $\lambda 8183, 8185 \text{ \AA}$ and MgI: $\lambda 8807 \text{ \AA}$. The strengths of the NaI and MgI lines are used as proxies for surface gravity to evaluate membership in W1. We model these lines as a double or single Gaussian, respectively, and integrate the resulting fitted parameters to determine equivalent widths. These quantities are used at the end of §3.1 to validate membership selection.

We measure the equivalent width of the Ca II triplet (CaT) lines ($\lambda 8498, 8542, 8662 \text{ \AA}$) as described in Geha et al. (2026). We simultaneously model the CaT lines with a Gaussian-plus-Lorentzian profile (for stars at $S/N > 15$ per spectral pixel) or a Gaussian profile (for stars at $S/N < 15$ per spectral pixel). We integrate the resulting fits to determine total equivalent width, which we refer to as CaT. From these CaT EW measurements, we derived [Fe/H] measurements for all candidate RGB stars ($M_V < 3$) assuming the empirical luminosity-dependent EW-[Fe/H] calibration from Navabi et al. (2026) which is an update to the Carrera et al. (2013) calibration using the same functional form. We adopt the form of the calibration based on the absolute V -band magnitude of each star, which we estimate by transforming our MegaCam $g-$ and $r-$ band photometry (see §2.3). As detailed in Geha et al. (2026), an error floor of 0.05 \AA is added to the CaT measurements based on repeat measurements, while a 0.1 dex error floor is included in the [Fe/H] values to account for inherent scatter in the Navabi et al. calibration itself, noting this term dominates at $S/N > 25$.

2.3. Ground-based Imaging and Matching to Gaia

We require photometry for all kinematic measurements to assess membership in W1 (see Figure 2, top panel). We use the Canada-France-Hawaii Telescopes (CFHT) MegaCam photometric catalog from Muñoz et al. (2018a) and adopt the fitted density profile and structural parameters from this analysis (see Table 2). These data are a full magnitude deeper than that available from the DESI Legacy Imaging Surveys DR9 (Dey et al. 2019). The Muñoz et al. (2018a) $g-$ and $r-$ band magnitudes are corrected for foreground Galactic extinction using Schlegel et al. (1998). Given the small magnitude uncertainties reported by Muñoz et al. (2018a) ($< 0.01 \text{ mag}$), we add a systematic photometric uncertainty of 0.02 mag in quadrature.

A important improvement to previous studies of W1 is the available Gaia DR3 catalogue (Gaia Collaboration et al.

Table 1. Summary of Willman 1 Keck/DEIMOS Observations.

Mask	Date	N_{exp}	Σt_{exp}	PIs	Slit width	N_{slits}	$N_{\text{good}}/N_{\text{slits}}$	Reference
203WiSB	20060527	3	3600	<i>Chapman</i>	0.7	63	0.62	Martin et al. (2007)
W1_1	20061120	5	9000	<i>Brodie</i>	1.0	113	0.48	Willman et al. (2011)
W1_2	20061121	5	9000	<i>Brodie</i>	1.0	101	0.38	Willman et al. (2011)
W1_3	20061122	3	5400	<i>Brodie</i>	1.0	92	0.41	Willman et al. (2011)
W1_4	20070320	3	5400	<i>Brodie</i>	0.7	123	0.07	Willman et al. (2011)
W1_5	20170425	7	12000	<i>Geha</i>	0.7	71	0.28	New Data; this work
W1_6	20170426	5	9000	<i>Geha</i>	0.7	66	0.42	New Data; this work
W1_9	20210408	5	9000	<i>Geha</i>	0.7	70	0.4	New Data; this work
Will1_1B	20230124	6	7200	<i>Rich</i>	0.8	39	0.38	New Data; this work
will1_5	20230124	6	7200	<i>Rich</i>	0.8	33	0.45	New Data; this work
Will1_2B	20230125	6	7200	<i>Rich</i>	0.8	31	0.42	New Data; this work
will1_6	20230125	6	7200	<i>Rich</i>	0.8	29	0.34	New Data; this work

NOTE—List of DEIMOS masks present in this work. (1) DEIMOS mask name, (2) date observed, (3) number of exposures reduced in this work, (4) total integrated exposure time, (5) Principal Investigator (PI) name, (6) slit width, (7) number of slits in a mask, (8) fraction of targeted objects in a mask with a measured velocity, (9) Published reference.

2023). While *Gaia* will only cover W1 stars above the sub-giant branch ($r \lesssim 20$), it significantly reduces contamination in this region due to the addition of proper motion and parallax measurements. We match our DEIMOS catalog to *Gaia* DR3 with a 1.5'' matching radius, resulting in 65 matches that are considered for membership.

3. MEMBERSHIP SAMPLE

Assessing whether a given star belongs to W1 or is part of the foreground Milky Way is particularly challenging because of the kinematic overlap between these two populations. We begin by describing our membership assessment method (§3.1). We then present our final member sample and compare to previous member samples in the literature (§3.2).

3.1. Membership Determination

To evaluate the likelihood that a given star is a member of W1, we assess five criteria for membership: (1) the star's position on the CMD, P_{CMD} ; (2) the star's heliocentric radial velocity, P_{vel} ; (3) the star's proper motion, P_{pm} ; (4) the star's parallax, P_{parallax} ; and (5) the star's [Fe/H] iron abundance, $P_{[\text{Fe}/\text{H}]}$. Criteria (3) and (4) are only considered for stars with parallax and proper motion measurements available from *Gaia* DR3 (Gaia Collaboration et al. 2023, see §2.3).

Due to tentative evidence for multi-directional tails and tidal stripping (Martin et al. 2007; Willman et al. 2011), no spatial cuts were performed on the data as to not introduce assumptions about W1's spatial spread of stars, although we limit our sample to $3 r_{\text{half,ell}}$ to determine physical properties (see §4). We additionally consider two surface gravity indi-

cators (NaI and MgI), but find these do not improve membership discrimination for the case of W1 and discuss this below. The membership probability, P_{mem} , of a star is defined as the product of all five criteria (Figure 1):

$$P_{\text{mem}} \propto P_{\text{CMD}} \times P_{\text{vel}} \times P_{\text{pm}} \times P_{\text{parallax}} \times P_{[\text{Fe}/\text{H}]} \quad (1)$$

We next describe in more detail each of these terms.

P_{CMD} is determined by comparing each star's position on the CMD to an old, metal-poor isochrone from the PARSEC stellar evolutionary track models ($\tau = 12$ Gyr, $\text{Fe}/\text{H} = -2.1$, Bressan et al. 2012). We use the updated distance value of 38.55 ± 0.45 based on *HST* imaging from Durbin et al. (2025, uncertainty via private communication). This value is consistent with that measured in Willman et al. (2011, 38 ± 7 kpc). We use this to calculate the minimum distance between the isochrone and the star's location on the CMD. This distance (d_{\min}) and the overall magnitude uncertainty of the star (δ_{mag} , the quadrature sum of the r -band and g -band magnitude uncertainty), are then used to evaluate the star's CMD membership probability, P_{CMD} (see Figure 1a):

$$P_{\text{CMD}} = \exp \left(-\frac{d_{\min}^2}{2[\sigma_{\text{CMD}}^2 + \delta_{\text{mag}}^2]} \right), \quad (2)$$

where σ_{CMD} is set to 0.15 mag. This CMD spread was roughly estimated from the span of other possible isochrones with varying ages and metallicities ($\tau = 8$ to 13 Gyr, $[\text{Fe}/\text{H}] = -1.9$ to -2.3) to account for the uncertainty in both parameters.

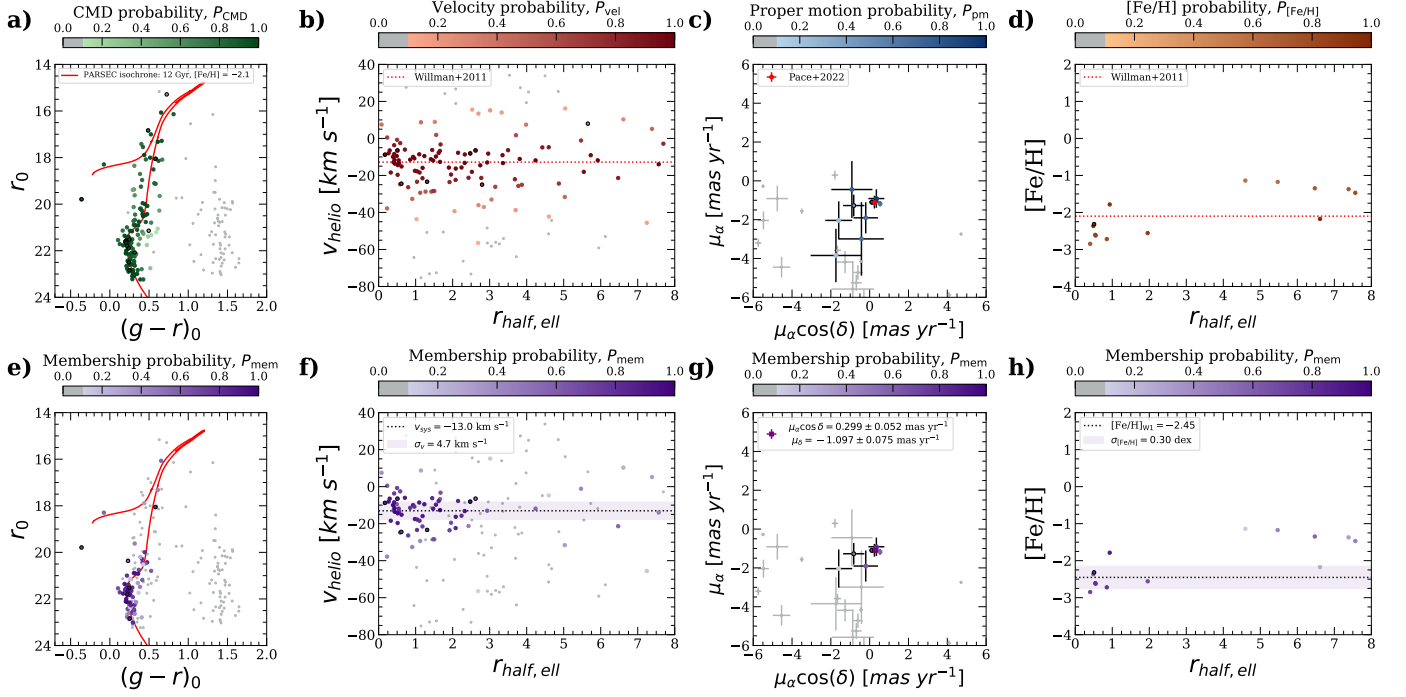


Figure 1. From our five criteria for membership (panels *a*, *b*, *c*, *d*), the membership probability of each star was determined (panels *e*, *f*, *g*, *h*). In each plot (*left to right*: CMD, velocity, proper motion, and metallicity profile), all stars with photometric and radial velocity measurements are color-coded according to the membership probability of the criterion in question, with clear non-members ($P_{\text{criterion}} < 0.1$) colored gray. Stars with variable velocities are circled in black. The priors for each marker are delineated in the top panels (Willman et al. 2011; Pace et al. 2022), and the properties derived from our member sample are shown in the bottom panels (see §4, Table 2).

319 P_{vel} is based on each star’s heliocentric, line-of-sight
320 velocity and, for consistency’s sake, is calculated using a simi-
321 lar probability distribution as P_{CMD} . For a star with velocity
322 $v \pm \delta_v$, its membership probability based on velocity, P_{vel} , is
323 calculated as (see Figure 1b):

$$324 P_{vel} = \exp\left(-\frac{(v - v_{W1})^2}{2[(3\sigma_v)^2 + \delta_v^2]}\right), \quad (3)$$

325 where $v_{W1} = -12.8 \text{ km s}^{-1}$, the systemic velocity of W1,
326 and $\sigma_v = 4.8 \text{ km s}^{-1}$, the velocity dispersion of W1, as de-
327 termined by Willman et al. (2011). We multiply the velocity
328 dispersion by three to loosen the distribution and avoid arti-
329 ficially biasing the sample towards the priors.

330 For stars with measured *Gaia* proper motions and paral-
331 laxes, the corresponding membership probabilities for each
332 of these quantities, P_{pm} and P_{parallax} , were determined. Pace
333 et al. (2022) report proper motion values of $(\mu_{\alpha,W1}^*, \mu_{\delta,W1}) =$
334 $(0.255 \pm 0.085, -1.110 \pm 0.096) \text{ mas yr}^{-1}$ for W1 based
335 on *Gaia* EDR3 astrometry. For a star with proper motion
336 $(\mu_{\alpha}^*, \mu_{\delta})$ and overall proper motion uncertainty δ_{pm} (calcu-
337 lated by summing the two dimensions in quadrature), the
338 membership probability based on proper motion, P_{pm} , is de-
339 fined as (see Figure 1c):

$$340 P_{pm} = \exp\left(-\frac{(\mu_{\alpha}^* - \mu_{\alpha,W1}^*)^2 + (\mu_{\delta} - \mu_{\delta,W1})^2}{2[(2\sigma_{pm})^2 + \delta_{pm}^2]}\right), \quad (4)$$

341 where σ_{pm} is the reported Pace et al. (2022) proper motion
342 uncertainties added in quadrature. Stars with a proper motion
343 uncertainty more than twice its signal value are treated as
344 non-measurements.

345 Situated at a distance of ~ 39 kpc, the parallax of W1 is
346 immeasurable by *Gaia*. As we find that the proper motion
347 membership criteria cleans the sample for the brightest stars,
348 we opt for a simple binary parallax marker: The parallax
349 membership probability is defined as $P_{\text{parallax}} = 1$ for stars
350 with parallax-over-error is less than 3 and $P_{\text{parallax}} = 0$ for
351 stars with parallax-over-error is greater than 3.

352 Finally, $P_{[Fe/H]}$ is determined from the CaT-based metal-
353 licity, $[Fe/H]$, for each star. Similar to the other markers, we
354 determine the metallicity membership probability for a star
355 with iron abundance $[Fe/H] \pm \delta_{[Fe/H]}$ as (see Figure 1d):

$$356 P_{[Fe/H]} = \exp\left(-\frac{([Fe/H] - [Fe/H]_{W1})^2}{2[(2\sigma_{[Fe/H]})^2 + \delta_{[Fe/H]}^2]}\right), \quad (5)$$

357 where $[Fe/H]_{W1} = -2.1$, the mean spectroscopic metallicity
358 of W1, and $\sigma_{[Fe/H]} = 0.45 \text{ dex}$, half the distance between the
359 most metal-poor and metal-rich star in the three star spectro-
360 scopic sample of Willman et al. (2011). This measurement
361 was chosen as our prior as it is the largest member sample
362 available with spectroscopic metallicity measurements.

363 Beyond these five parameters, there are a few spectral lines
364 covered by DEIMOS that can be incorporated into member-

ship selection to further differentiate between member stars and Milky Way dwarf star contaminants. The NaI absorption line at 8234 Å correlates with surface gravity and can be used to identify Milky Way dwarf stars which display systematically stronger lines than giants (Schiavon et al. 1997). All stars with $P_{\text{mem}} > 0.5$ have small NaI equivalent widths ($< 1 \text{ \AA}$ within $1-\sigma$). Alternatively, Battaglia & Starkenburg (2012) identified a distinction line between RGB stars and dwarf stars in the equivalent width of the MgI line at 8806.8 Å as a function of the equivalent width of the CaT lines that can also be used to cut Milky Way dwarf star interlopers. Again, all stars with $P_{\text{mem}} > 0.5$ lie within $1-\sigma$ of the cut-off line, a result that is consistent with the predictions for a metal-poor system. While the use of these NaI and MgI lines are redundant and do not add more layers to our membership selection, they are a useful tool for validating that our selection criterion are efficiently differentiating between W1 members and Milky Way foreground stars.

3.2. Final Member Sample and Comparison to Literature Samples

The membership probability, P_{mem} , of each star is shown in the bottom panels of Figure 1. From this, we define stars with $P_{\text{mem}} > 0.5$ as members of W1. This results in 57 members, all but 1 of which lie within $3 r_{\text{half,ell}}$. We recognize the subjectiveness of this probability cut-off and take this into account when calculating the properties of W1 (see §4.1). Multiple velocity epochs exist for 36 of the 57 stars in our sample, from which we identify 6 velocity variables including 1 blue straggler. We infer the physical parameters of W1 from the 49 members within $3 r_{\text{half,ell}}$, and these properties are presented in Table 2.

As shown in Figure 2, we report that 28 members are inside the elliptical half-light radius, 19 of which have multiple velocity epochs and non-variable velocities. We highlight that, despite implementing no spatial cuts, the stellar density distribution of our member sample shows no stars in excess of a Plummer profile. The CMD of W1 members is consistent with that of an old, metal-poor system, and we identify eight RGB stars for which we measure spectroscopic metallicities.

All 45 published members in Willman et al. (2011) overlap with the Keck/DEIMOS spectroscopy within $1.5''$. Due to more stringent quality criteria, seven stars in the 2011 sample have no velocity measurements in this work due to low S/N and poor velocity fits and were thus not considered for membership. A total of 31 stars in the 2011 sample overlap with the 57 member stars in this work. The seven remaining stars in the 2011 sample are labeled as non-members: four on the basis of proper motion/parallax estimates from *Gaia* and three due to updated velocities that are inconsistent with the systemic motion of W1. We also find the presence of four stars flagged as velocity variables by this work in the 2011

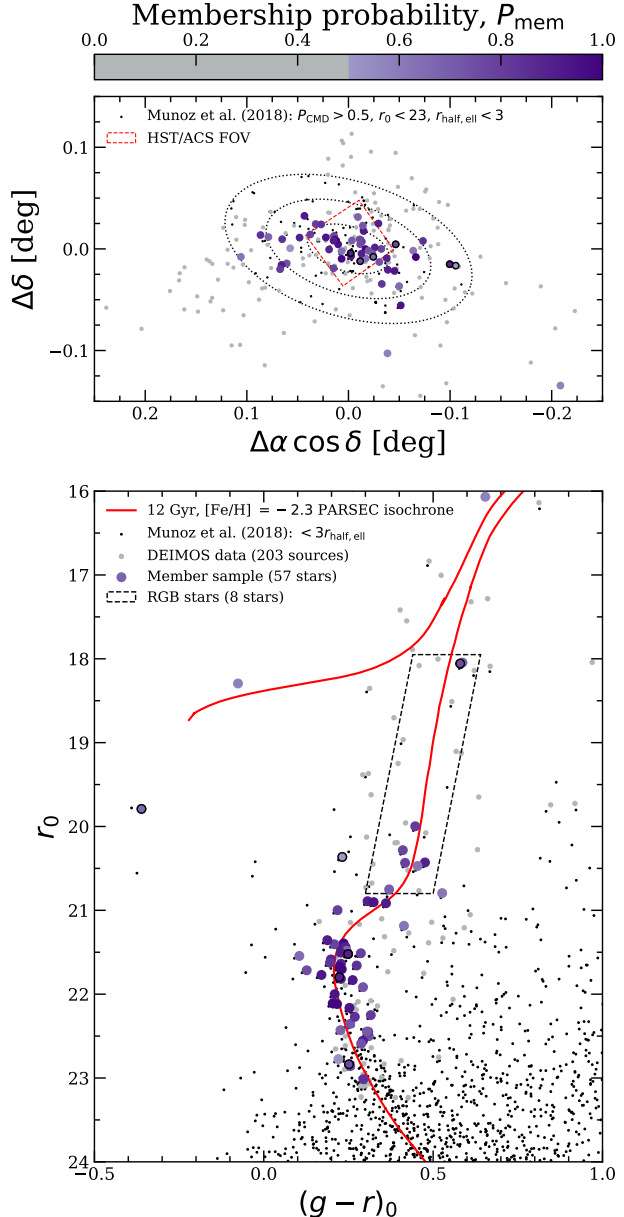


Figure 2. Upper: Spatial distribution of the 57 W1 member stars, color-coded according to P_{mem} . Members with variable velocities are circled in black and non-members are in colored gray. The three concentric dotted ellipses represent the space within 1, 2, and 3 $r_{\text{half,ell}}$. All stars with photometry from Muñoz et al. (2018a) within $3 r_{\text{half,ell}}$, $P_{\text{CMD}} > 0.5$, and $r_0 < 23$ are shown in black. The field of view of the *HST/ACS* imaging is denoted red (see §5.1). Lower: CMD of W1 member stars overlaid with an old, metal-poor PARSEC isochrone in red. All stars with photometry from Muñoz et al. (2018a) within $3 r_{\text{half,ell}}$ are shown in black. The liberally defined red giant branch for which we measure spectroscopic metallicities is boxed.

sample. Of the 52 foreground Milky Way stars reported in Willman et al. (2011), 51 stars have matches with our measured velocities. One of these stars is included in our member

Table 2. Properties of Willman 1.

Parameter	Value	Units	Reference
α_{J2000}	162.3436	deg	Muñoz et al. (2018a)
δ_{J2000}	51.0501	deg	Muñoz et al. (2018a)
D_\odot	38.55 ± 0.45	kpc	Durbin et al. (2025) ^a
$(m - M)_0$	17.93 ± 0.03	mag	Durbin et al. (2025) ^a
r_{half}	2.51 ± 0.22	arcmin	Muñoz et al. (2018b)
r_{half}	26.8 ± 3.2	pc	Muñoz et al. (2018b)
ϵ	0.47	—	Muñoz et al. (2018b)
Position angle	73	deg	Muñoz et al. (2018b)
M_V	-2.56 ± 0.74	mag	Muñoz et al. (2018b)
L_V	888 ± 605	$L_{V,\odot}$	Muñoz et al. (2018b)
v_{sys}	$-13.0^{+1.1}_{-1.1}$	km s^{-1}	§4.1
σ_v	$4.7^{+1.5}_{-1.3}$	km s^{-1}	§4.1 ^b
$M_{1/2}$	$5.9^{+3.7}_{-3.4} \times 10^5$	M_\odot	§4.1
$(M/L)_{V,1/2}$	660 ± 590	$M_\odot/L_{V,\odot}$	§4.1
[Fe/H]	$-2.45^{+0.12}_{-0.13}$	—	§4.2
$\sigma_{\text{[Fe/H]}}$	$0.30^{+0.15}_{-0.11}$	dex	§4.2
μ_α^*	0.299 ± 0.052	mas yr^{-1}	§6.1
μ_δ	-1.097 ± 0.075	mas yr^{-1}	§6.1
r_{peri}	$14.7^{+1.9}_{-1.6}$	kpc	§6.1 ^c
r_{apo}	$43.2^{+0.5}_{-0.5}$	kpc	§6.1 ^c
e	$0.49^{+0.04}_{-0.05}$	—	§6.1 ^c

NOTE—List of global structural, kinematic, chemical, and orbital parameters of W1.

^aThe reported distance/distance modulus uncertainty is likely underestimated as it does not include the systematic contributions from isochrones.

^bWe opt to cite the velocity dispersion determined from our two-component Gaussian mixture model as it incorporates the uncertainty in membership.

^cWe report the orbital properties determined from MWPotential2014 of Bovy (2015), with the dark matter halo mass scaled up by 50% and the addition of the LMC.

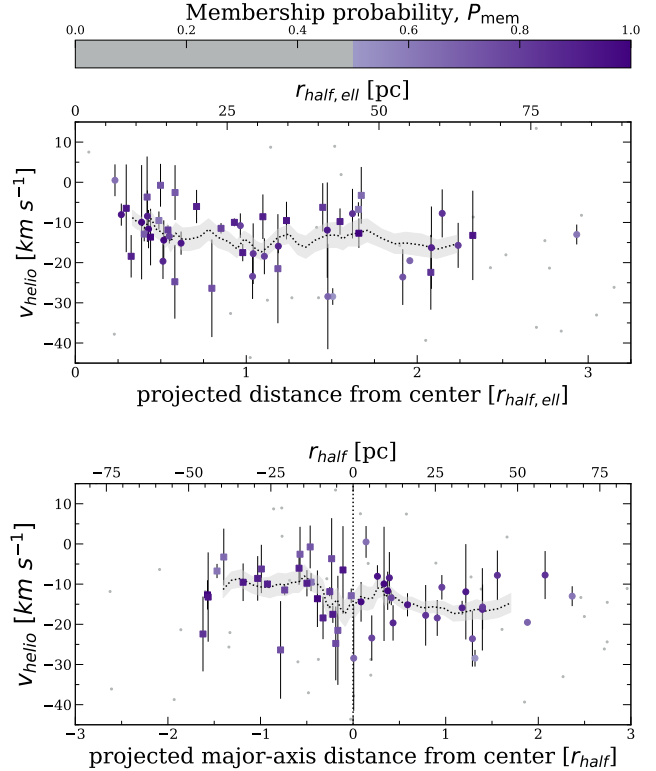


Figure 3. Heliocentric radial velocities and uncertainties of the 49 members as a function of elliptical half-light radius (*upper*) and projected distance with respect to the major axis (*lower*). For both plots, stars to the left and the right of the center axis of W1 are plotted as squares and circles, respectively. All 49 stars are color-coded purple according to their membership probability and non-members are in gray. In both panels, the dotted black line represents the membership probability weighted 7-star rolling velocity average, and the gray shaded region represents the uncertainty in the rolling average calculated via bootstrapping.

4. RESULTS

With a sample of 49 W1 members within $3 r_{\text{half,ell}}$ with measured velocities, we next probe the **kinematic** (§4.1) and **chemical** (§4.2) properties of this system.

4.1. Velocity Dispersion and Dynamical Mass

Based on our member sample, we present the velocity profile of W1 in Figure 3. Willman et al. (2011) reported a peculiar velocity profile where stars within $\sim 0.75 r_{\text{half,ell}}$ are offset from those in the outskirts, which they note as difficult to explain with an equilibrium model. This phenomenon is still observed by visual inspection in our updated member sample (see Figure 3, upper panel). Quantitatively, the rolling average decreases by about $8.5 \pm 3.0 \text{ km s}^{-1}$ from the center to the outskirts of W1. We find that this gradient is not obviously explained by ordered rotation (see Figure 3, lower panel).

We calculate the systemic velocity and velocity dispersion of W1 using a two-component Gaussian mixture model to simultaneously model the Milky Way and W1. We opt for this approach as it separates the two populations without imposing a strict membership threshold, allowing the inferred velocity dispersion to marginalize over contamination from Milky Way foreground stars (e.g., Martinez et al. 2011).

We begin by eliminating obvious non-members from our full dataset using the membership probabilities determined in §3.1. We define obvious non-members as stars whose membership probability without velocity ($P_{\text{mem,nov}} \propto P_{\text{CMD}} \times P_{\text{pm}} \times P_{\text{parallax}} \times P_{[\text{Fe}/\text{H}]}^*$) is less than 0.1 or stars with large radial velocities ($|v| > 150 \text{ km s}^{-1}$). This results in 65 stars within $3 r_{\text{half,ell}}$. Our results are not sensitive to our membership or velocity cut-off choices **within the reported uncertainties**. We then apply a two-component Gaussian maximum likelihood function, whose total log likelihood takes the form (Walker et al. 2006):

$$\ln \mathcal{L} = \sum_i \ln [f \cdot \mathcal{N}(v_i | v_{\text{W1}}, \sigma_{\text{W1}}^2 + \delta v_i^2) + (1 - f) \cdot \mathcal{N}(v_i | v_{\text{MW}}, \sigma_{\text{MW}}^2 + \delta v_i^2)],$$

where f is the fraction of W1 members in our dataset, v_{W1} is the systemic velocity of W1, σ_{W1} is the velocity dispersion of W1, v_{MW} is the systemic velocity of the Milky Way, and σ_{MW} is the velocity dispersion of the Milky Way. We account for the velocity measurement uncertainty of each star, δv_i , by adding it in quadrature to the intrinsic dispersion of each Gaussian.

To sample this model, the MCMC sampler `emcee` (Foreman-Mackey et al. 2013) was run using 20 walkers. We initialize our walkers with the values from Willman et al. (2011) for W1 ($v_{\text{W1}} = -12.8 \text{ km s}^{-1}$, $\sigma_{\text{W1}} = 4.8 \text{ km s}^{-1}$), reasonable values for the Milky Way ($v_{\text{MW}} = 0 \text{ km s}^{-1}$, $\sigma_{\text{W1}} = 50 \text{ km s}^{-1}$), and a member fraction equivalent to the fraction of our determined member sample ($f = 0.75$), but our results are not dependent on these choices. We adopt the following uniform priors for our five parameters: $-100 < v_{\text{MW}} < 100 \text{ km s}^{-1}$, $0 < \sigma_{\text{MW}} < 200 \text{ km s}^{-1}$, $-30 < v_{\text{W1}} < 10 \text{ km s}^{-1}$, $0 < \sigma_{\text{W1}} < 10 \text{ km s}^{-1}$, $0 < f < 1$. The distribution of posterior samples is shown in the upper panel of Figure 4. We measure the systemic velocity as the sample median and the associated uncertainties from 16th and 84th percentiles.

The systemic velocity of W1 is estimated to be $v_{\text{sys}} = -13.0^{+1.1}_{-1.1} \text{ km s}^{-1}$ with a velocity dispersion of $\sigma_v = 4.7^{+1.5}_{-1.3} \text{ km s}^{-1}$, which is consistent with measurements by Willman et al. (2011) and Geha (2026). We highlight that the velocity dispersion is degenerate with the member fraction, implying that the large uncertainty in W1's velocity dispersion is driven by the uncertainty in identifying a pure member sam-

ple. This result is unchanged within the reported uncertainty when restricting the sample to anywhere within 2 to 4 $r_{\text{half,ell}}$, or when restricting the sample to only stars with multiple velocity epochs. When cutting the sample to $1 r_{\text{half,ell}}$, the uncertainty on the velocity dispersion grows such that the system is not conclusively resolved due to the small sample size of stars. Notably, the kinematic distribution of W1 is asymmetric and non-Gaussian, suggesting that a single global velocity dispersion value is insufficient to fully characterize the complex kinematic profile of W1 (see Figure 4, bottom panel).

Assuming dynamical equilibrium, the dynamical mass of W1 within its half-light radius can be inferred from this radial velocity dispersion. Following the methods of Wolf et al. (2010), the mass of W1 within the half-light radius is estimated to be $5.9^{+3.7}_{-3.4} \times 10^5 M_{\odot}$, corresponding to a central mass-to-light ratio of $(M/L)_V = 660 \pm 590$. This is consistent with the dynamical mass and mass-to-light ratio previously determined by Willman et al. (2011) ($\sim 3.9^{+2.5}_{-1.6} \times 10^5 M_{\odot}$; $(M/L)_V = 770^{+930}_{-440}$; note that we use an updated M_V value causing the mass-to-light ratio in this work to be smaller despite a larger mass).

The member fraction estimated from our mixture model is $f = 0.74^{+0.07}_{-0.08}$, which is consistent with the number of members determined in §3. We find **similar** results when employing a single Gaussian maximum likelihood model on our member sample of 49 stars within $3 r_{\text{half,ell}}$. From this method, the systemic velocity of W1 is measured to be $v_{\text{sys}} = -12.8^{+1.0}_{-1.0} \text{ km s}^{-1}$ with a velocity dispersion of $\sigma_v = 4.8^{+0.9}_{-0.8} \text{ km s}^{-1}$. Requiring multiple velocity epochs or reducing the half-light radius cut-off down to $2 r_{\text{half,ell}}$ does not alter the systemic velocity or velocity dispersion beyond the uncertainties determined. These results are consistent with the two-component Gaussian, but with likely underestimated uncertainties. As such, we emphasize our values from the mixture model which incorporate the uncertainty in membership as well. **Table A3 presents the measured properties of all 73 stars considered in our analysis, including the 65 stars used in the mixture model and the 57 stars in the final member sample.**

4.2. Metallicity Distribution

As detailed in §2.2, we are able to infer [Fe/H] measurements for the stars in our member sample based on CaT equivalent width measurements. This calibration is only valid for RGB stars ($M_V < 3$), significantly reducing our member sample to **eight** stars with measured metallicities, **all of which are within $2 r_{\text{half,ell}}$** (see Figure 2, lower panel; Figure 5, upper panel). From this sample, we determine the CaT-based mean metallicity and metallicity dispersion using an MCMC sampler with 20 walkers to sample from a Gaussian maximum likelihood function (Foreman-Mackey et al.

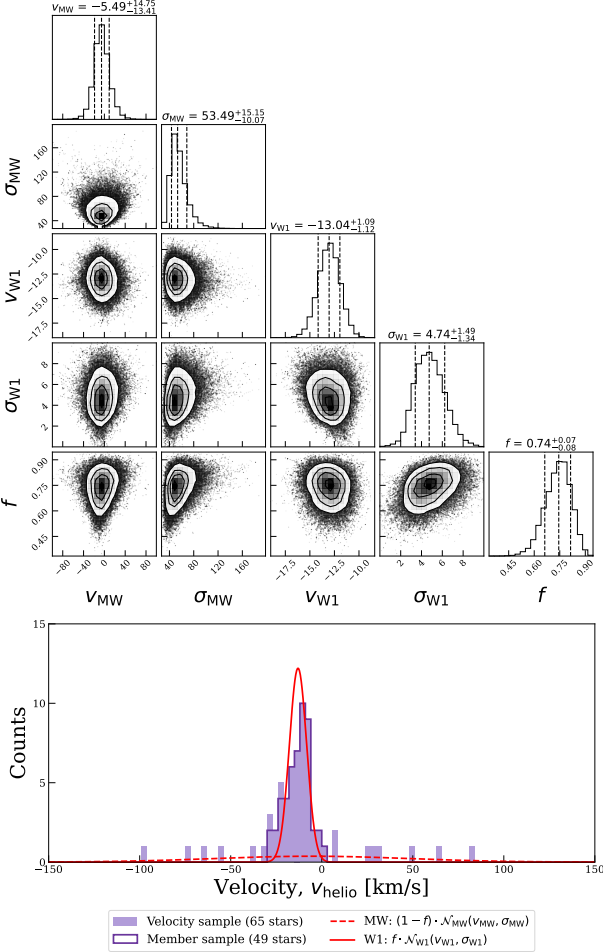


Figure 4. *Upper:* Posterior samples for the two-component Gaussian mixture model to measure the systemic velocity and velocity dispersion of W1 based on a velocity sample of 65 potential member stars within $3 r_{\text{half,ell}}$. The dashed lines represent the median value and 16th and 84th percentiles. *Lower:* Best-fit mixture model of two-component Gaussian representing the Milky Way and W1. The 65 potential members used for our fitting are over-plotted, and the member sample (§3.2) is outlined in purple. We note the asymmetric velocity distribution and comment on this in §7.2.

2013; Walker et al. 2006). We opt not to use a mixture model as performed in §4.1 due to the small sample size (see Figure 1h). We initialize our walkers using the values determined by Willman et al. (2011) ($[\text{Fe}/\text{H}] = -2.1$, $\sigma_{[\text{Fe}/\text{H}]} = 0.45$ dex). The median and 16th and 84th percentiles of the resulting posterior distribution function are presented.

The metallicity of W1 is measured to be $[\text{Fe}/\text{H}] = -2.45^{+0.12}_{-0.13}$ with a metallicity dispersion of $\sigma_{[\text{Fe}/\text{H}]} = 0.30^{+0.15}_{-0.11}$ dex (see Figure 5). The removal of the highest metallicity star slightly lowers the measured average metallicity and substantially reduces the measured metallicity spread (to $[\text{Fe}/\text{H}] = -2.53^{+0.08}_{-0.09}$, $\sigma_{[\text{Fe}/\text{H}]} = 0.12^{+0.12}_{-0.08}$ dex). We emphasize that this star has a high membership probabil-

ity ($P_{\text{mem}} \sim 0.9$) and that the mean metallicity without this star is still within the uncertainties derived with the full sample.

Willman et al. (2011) measured a metallicity spread in W1 based on Keck/DEIMOS spectroscopy of three RGB members ($[\text{Fe}/\text{H}] = -1.73 \pm 0.12$, -2.65 ± 0.12 , and -1.92 ± 0.21). These three stars are in our member sample, although we report slightly lower metallicity values for two of these stars ($[\text{Fe}/\text{H}] = -2.32 \pm 0.13$, -2.56 ± 0.13 , and -2.61 ± 0.19 , respectively). In comparison with the photometric metallicity values derived from *HST* CaHK imaging from Fu et al. (2023) ($[\text{Fe}/\text{H}] = -2.53^{+0.11}_{-0.11}$, $\sigma_{[\text{Fe}/\text{H}]} = 0.65^{+0.10}_{-0.09}$ dex), we measure W1 to be a slightly more metal-rich system with a substantially smaller metallicity dispersion.

5. MASS SEGREGATION

We now shift our attention to the *HST/ACS* data (§5.1), evaluating the presence of stellar mass segregation which can be used to differentiate between a galactic and star cluster origin for W1 (§5.2).

5.1. *HST/ACS Imaging*

W1 was observed by the *Hubble Space Telescope* (*HST*) in 2017 as part of the Treasury Program GO-14734 (PI-Kallivayalil). Deep photometry of W1 was obtained with the Advanced Camera for Surveys (ACS; Ford et al. 1998) using the Wide Field Channel (WFC). The ACS/WFC field approximately covers the inner half-light radius of W1 (see Figure 2, upper panel). Observations were split evenly between the F606W and F814W filters with a combined exposure time of 9254 seconds.

For the analysis below, we use the same *HST* data reduction as described in Richstein et al. (2024). Briefly, the individual exposures from each filter were aligned and co-added using DrizzlePac, an *HST* software package. The combined output images were then masked with the segmentation routine from the photutils package (Bradley et al. 2025). PSF-fitting photometry was performed on the combined images using DAOPHOT-II and ALLSTAR (Stetson 1987, 1992). The source lists from F606W and F814W were matched using DAOMATCH and DAOMASTER to create a preliminary PSF source catalog. An empirically-derived aperture correction was applied to the magnitudes, which were then converted to the VegaMag system and adjusted for the exposure time. Finally, to address star-galaxy separation, each source was assigned a quality flag from 0 to 1 based on how closely its parameters matched those in artificial star tests across different filters.

We also note that Durbin et al. (2025) used *HST* imaging to measure the star formation histories of 36 ultra-faint dwarf galaxies, including W1. Their results indicate that 50% of W1’s stellar mass formed $\tau_{50} = 13.44^{+0.00}_{-0.81}$ Gyr and 90% of

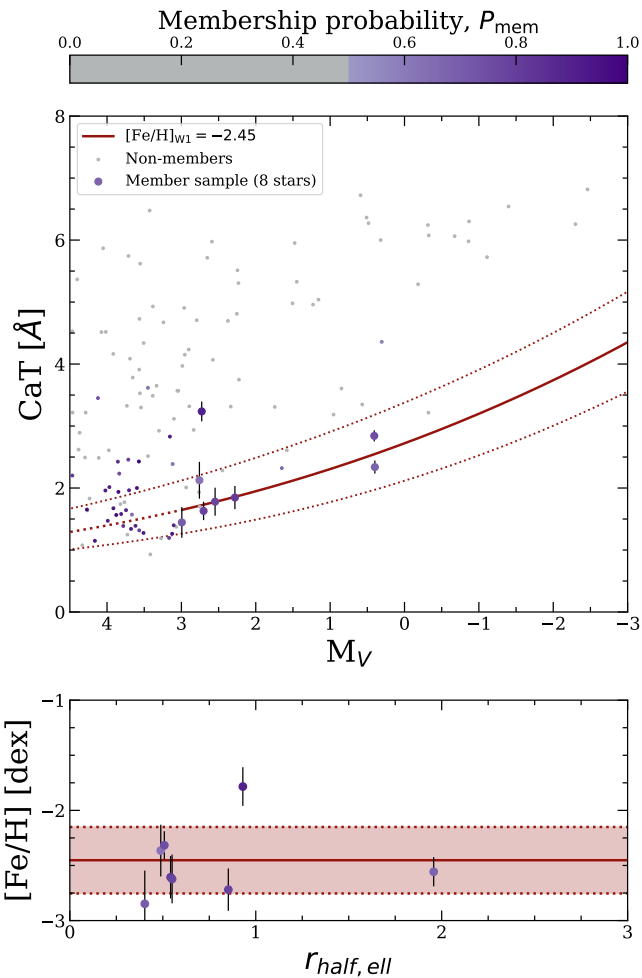


Figure 5. CaT equivalent width as a function of V-band magnitude (upper panel) and the CaT-based spatial metallicity distribution (lower panel) for the eight RGB stars in our member sample. The solid line denotes the calibration range of the empirical relationship of Carrera et al. (2013) plotted at the mean metallicity of W1 while the dotted lines represents the metallicity dispersion determined from MCMC sampling.

W1's stellar mass formed before $\tau_{90} = 8.37^{+0.08}_{-0.93}$ Gyr, indicating a uniformly ancient stellar population formed from an early burst of star formation. We obtain consistent results when performing a similar star formation history analysis on this dataset.

5.2. Mass Segregation Determination

The presence of mass segregation can be used as a diagnostic for determining whether a system is a star cluster or a dwarf galaxy (Baumgardt et al. 2022). Due to the equipartition of kinetic energy whereby high-mass stars transfer energy to low-mass stars over time, high-mass stars tend to aggregate near the center of systems while low-mass stars

drift towards the outer regions. This process occurs over the course of a few relaxation periods, and is thus a significant feature in old stellar objects with relatively short relaxation periods compared to their age, such as globular clusters (e.g., Tripathi et al. 2023; Kim et al. 2015; Weatherford et al. 2020). For systems with substantial amounts of dark matter such as ultra-faint dwarf galaxies, the system's relaxation period is prolonged beyond a Hubble time such that mass segregation is unobservable (Longeard et al. 2018).

Baumgardt et al. (2022) first evaluated the presence of mass segregation in W1 using an independent reduction of the same *HST/ACS* imaging. They compared the cumulative radial distribution of stars in the upper and lower regions of the main sequence, constructing two samples: one of bright, higher-mass stars and the other of faint, lower-mass stars. In highly segregated systems, such as globular clusters, the ratio of half-light radii for these two samples usually lies around 0.7. For W1, Baumgardt et al. (2022) measured a ratio of $R_{\text{half,bright}}/R_{\text{half,faint}} = 1.05 \pm 0.08$, indicating a lack of mass segregation and evidence towards a dwarf galaxy classification.

Loosely following the methods of Baumgardt et al. (2022), we re-analyze the same *HST/ACS* data to rigorously evaluate the possibility of mass segregation in W1. We begin by removing extragalactic sources, defined as those with star quality flags > 0.7 . To isolate the probable member stars in W1, we compared the CMD of the 1,055 remaining stars to an old, metal-poor isochrone from the MIST stellar evolutionary track models ($\tau = 12$ Gyr, $[\text{Fe}/\text{H}] = -2$, shifted to a distance modulus of $m - M = 17.93$ which corresponds to a distance of 38.55 kpc), accounting for interstellar reddening (Dotter 2016; Choi et al. 2016; Sirianni et al. 2005; Schlegel et al. 1998). We define members as stars with the greater of either 0.15 mag or twice their photometric uncertainty from the isochrone. Finally, due to the limited field of view of the ACS/WFC compared to the extended spatial distribution of W1, only stars contained within $1 r_{\text{half,ell}}$ were included to ensure that the mass segregation profile was not controlled by just a few outlying stars. Our final sample consists of 635 stars.

We first use the MS turnoff and the estimated location of $0.5M_\odot$ stars included in the synthetic isochrone as upper and lower photometric bounds. The stars that passed the spatial and CMD cuts within these bounds were divided into two groups of equal size based on stellar brightness to create two separate samples of bright and faint stars (see Figure 6, upper left panel). The radial cumulative distribution of stars for each sample was determined using an elliptical aperture with half-light radius, position angle, and ellipticity values from Martin et al. (2008) (see Table 2). The half-light radius for each sample was defined as the elliptical radius within which half of the stars of each sample are contained.

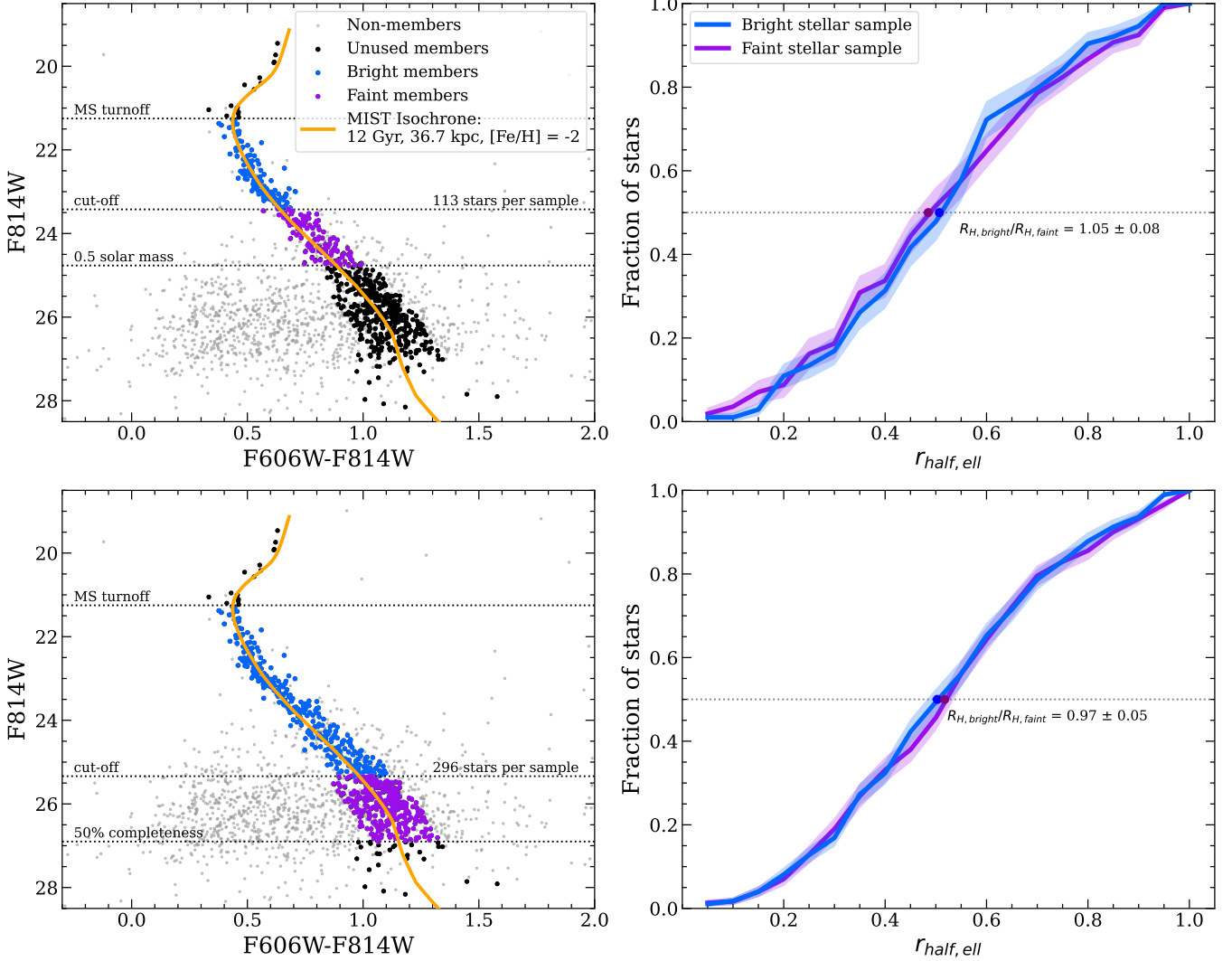


Figure 6. Mass segregation analysis of W1 from *HST*/ACS observations. *Left:* CMD of W1 *HST* data overlaid with an old, metal-poor MIST isochrone in orange. Blue and purple stars show the stars selected based on different magnitude cuts (*upper* = $0.5M_{\odot}$; *lower* = 50% completeness threshold) to calculate the mass segregation profile. *Right:* Corresponding average cumulative elliptical radial distribution of stars. The shaded region corresponds to the $1-\sigma$ uncertainty calculated by bootstrapping over each sample. No significant signs of mass segregation are detected.

Baumgardt et al. (2022) estimated that the expected half-light ratio between bright and faint stars for a star cluster the size of W1 is 0.90, a value which would only be more extreme if W1 is tidally disturbed as both mass segregation and tidal stripping would preferentially remove low-mass stars from the central regions (Paust et al. 2009). We obtained a half-light radius ratio of $R_{\text{half},\text{bright}}/R_{\text{half},\text{faint}} = 1.05 \pm 0.08$, where the uncertainty is calculated by bootstrapping over each sample (see Figure 6, upper right panel). A standard two-sample KS test shows a <1% probability of mass segregation, which we highlight as a more comprehensive test statistic that takes into account the full distributions rather than evaluating the discrepancy between distributions at a single location. This process was repeated using varying

lower bound cut-offs all the way down to the 50% photometric completeness limit (see Figure 6, bottom panels).

The results of these varied samples are consistent with an unsegregated system, with only a few samples showing inconclusive results (that is, with values compatible with both a segregated and unsegregated system). These results are unchanged by the use of a circular aperture, as originally performed by Baumgardt et al. (2022). All KS tests performed had probabilities of mass segregation less than 29.7%, the value determined by Baumgardt et al. (2022).

It should be noted that Willman et al. (2006) presented evidence for mass segregation using ground-based photometry to compare the luminosity function (LF) of stars in the central and tail regions. Observing an excess of low luminosity stars in the tail region, they performed a KS test that showed a 68%

chance that the two stellar LFs were drawn from different populations, which was interpreted as evidence for mass segregation. To revisit this claim using a larger sample size and deeper photometry, the 635 *HST* member stars were divided into two samples by implementing similar cuts to (Willman et al. 2006, Fig. 4): central stars within $0.5 r_{\text{half,ell}}$ and outer stars beyond $0.5 r_{\text{half,ell}}$. As carried out by Willman et al. (2006), the LF for each sample was determined and an offset value was added to the central region sample to correct for a difference in sample size and facilitate direct comparison. No surplus of low luminosity stars are observed in the outer stars and performing a two-sample KS test on the inner and outer sample LFs shows a $< 10\%$ probability that the two LFs were drawn from different populations, which we interpret as additional evidence that W1 is unsegregated. As one final check, this process was repeated for 57 member stars from our analysis of the DEIMOS data (§3.2), which also show no excess of low luminosity stars at the outskirts. Thus, we find no evidence for mass segregation in W1, consistent with the results of Baumgardt et al. (2022). This supports a dwarf galaxy classification for the system.

6. DYNAMICAL HISTORY

We next investigate the possibility of past tidal interactions between the Milky Way and W1 by examining the orbital history of W1 (§6.1) and simulating mock stellar streams (§6.2).

6.1. Orbit

We compute the orbit of W1 using the analytic potential **MWPotential2014** of the *galpy* package by Bovy (2015). This model of the Milky Way’s gravitational potential consists of a power-law spherical potential representing the bulge (Binney & Tremaine 1987), a Miyamoto-Nagai disk potential (Miyamoto & Nagai 1975), and a NFW dark matter halo potential (Navarro et al. 1997). From this, we integrate the orbit of W1 backwards in time based on its 6D phase-space coordinates (see Table 2 for values). We measure a proper motion of $(\mu_a^*, \mu_\delta) = (0.299 \pm 0.052, -1.097 \pm 0.075)$ mas yr⁻¹ by using a single Gaussian maximum likelihood model on the seven stars in our member sample with measured *Gaia* proper motions (see Figure 1g). This is consistent with the results of Pace et al. (2022), who apply background mixture models to *Gaia* EDR3 data, both in measurement value and the number of *Gaia* members.

Previous orbital analyses of Milky Way dwarf galaxies have reported moderately small pericenter distance values for W1 (ranging from 16 kpc to 44 kpc; Pace et al. 2022; Simon 2018; Armstrong et al. 2021), but are highly dependent on membership selection and the assumed Milky Way potential. To probe the effect of different assumed Milky Way potentials, we also model W1’s orbit using two other potentials. The estimated mass of the Milky Way’s dark matter

halo for **MWPotential2014** is on the lower end with a value of $0.8 \times 10^{12} M_\odot$. To account for this uncertainty, the second potential we adopt is the same **MWPotential2014** with a 50% larger dark matter halo mass ($1.2 \times 10^{12} M_\odot$). The Large Magellanic Cloud (LMC) has also been known to affect the orbits of objects, even those distant from it, due to the reflex-motion of the Milky Way’s orbit (e.g., Erkal et al. 2021; Ji et al. 2021; Correa Magnus & Vasiliev 2022; Patel et al. 2024). This MW+LMC potential is the third and final potential we use to calculate the orbit of W1, where the LMC is modeled by a moving Hernquist potential of mass $1.38 \times 10^{11} M_\odot$ and scale radius of 8.7 kpc, taking into account dynamical friction (Bovy 2015; van der Marel & Kallivayalil 2014; Hernquist 1990). We find the dynamical friction of W1 to have a negligible impact on its orbit. Due to uncertainty in orbit integration models beyond one orbital period (especially for satellites with pericenter distances < 30 kpc, D’Souza & Bell 2022; Machado et al. 2025), we use these potentials to model the 3-dimensional orbit of W1 over only the last 1 Gyr with a time resolution of 1 Myr.

Figure 7 compares the modeled orbits of W1 using these three different Milky Way potentials. The orbital period predicted by the original **MWPotential2014** is larger than the other two potentials by ~ 0.2 Gyr. In all cases, W1 is at apocenter, coming from a position closer to the Galactic center, although the exact pericenter distance of the orbit depends on the potential used.

Due to the uncertainties in distance, velocity, and proper motion measurements, the uncertainty in the orbit of W1 was calculated through Monte Carlo sampling. 1,000 six-dimensional phase-space coordinates were created by sampling distance, velocity, and proper motion values from Gaussian distributions based on each parameter’s average estimated value and $1-\sigma$ standard deviation (see Table 2). The reported distance uncertainty from Durbin et al. (2025) is likely underestimated as it does not include systematic contributions from the isochrones. Our orbital solutions remain conclusively consistent with a system moving away from a position closer in to the Milky Way up to distance uncertainties of ~ 3 kpc.

This procedure was performed for both the regular **MWPotential2014** and the potential with the addition of the LMC (see Figure 7). The orbit of W1 under the regular **MWPotential2014** has a pericenter distance of $r_{\text{peri}} = 24.9_{-3.1}^{+3.5}$ kpc, an apocenter distance of $r_{\text{apo}} = 43.5_{-0.5}^{+0.4}$ kpc, and an eccentricity $e = 0.27_{-0.06}^{+0.06}$. The addition of the LMC modifies these predictions, simulating a pericenter distance of $r_{\text{peri}} = 14.7_{-1.6}^{+1.9}$ kpc, an apocenter distance of $r_{\text{apo}} = 43.2_{-0.5}^{+0.5}$ kpc, and an eccentricity of $e = 0.49_{-0.05}^{+0.04}$. These reported parameters represent the median of our sampling procedure, and the uncertainties represent the 16th and 84th percentiles. None of the orbital samples for both potentials have pericen-

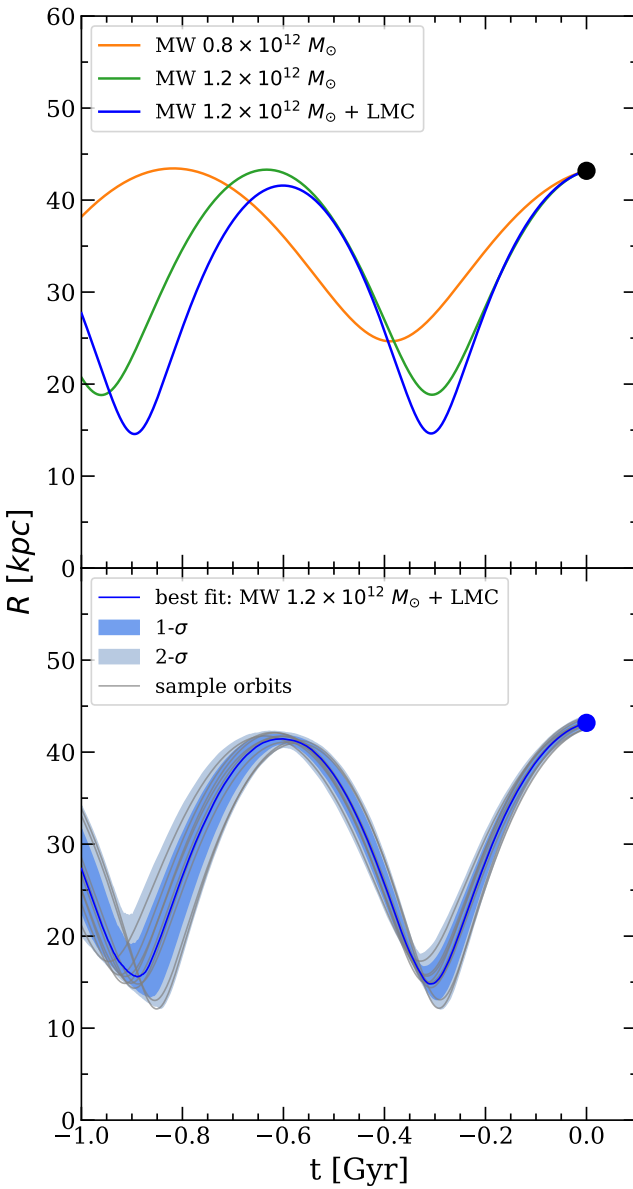


Figure 7. Orbit of W1. *Upper:* Distance of W1 to the galactic center as a function of time using three different Milky Way potentials from Bovy (2015) orbital simulations. *Lower:* Same as above but only showing the orbital simulations using MWPotential2014 of Bovy (2015), with the dark matter halo mass scaled up by 50% and the addition of the LMC. The blue line represents the 50th percentile orbit from Monte Carlo sampling over the 6D phase space parameter uncertainties; the dark blue shaded region represents the space within the 16th and 84th percentile orbits; and the light blue region represents the space between the 5th and 95th percentile orbits.

To quantitatively verify that W1 is at apocenter, we calculate the ratio f_{peri} of Fritz et al. (2018):

$$f_{\text{peri}} = \frac{r_{\text{GC}} - r_{\text{peri}}}{r_{\text{apo}} - r_{\text{peri}}}, \quad (6)$$

which is a proxy for the orbital phase in the radial direction. $f_{\text{peri}} = 0$ and 1 indicate an object at pericenter and apocenter, respectively. For both the regular MWPotential2014 and with the addition of the LMC, the ratio was determined to be $f_{\text{peri}} = 0.99 \pm 0.01$, consistent with our conclusion that W1 is being observed at or very near apocenter after spending time closer to the Galactic center.

From the estimate of the central dynamical mass of W1 (M_{W1}), the Jacobi tidal radius of W1 (R_J) as a function of orbital radius (R_{W1}) can be approximated (Innanen et al. 1983):

$$R_J(R) = \left(\frac{M_{\text{W1}}}{3M_{\text{MW}}} \right)^{1/3} R_{\text{W1}} \quad (7)$$

The mass of the Milky Way enclosed within the orbital radius of the satellite (M_{MW}) was determined from MWPotential2014 with a dark matter halo mass enlarged by 50% ($1.2 \times 10^{12} M_{\odot}$). From this, the current Jacobi tidal radius of W1 is estimated to be $R_J = 220^{+120}_{-140}$ pc, which corresponds to $7.7^{+1.6}_{-1.8}$ half-light radii. In comparison, the tidal radius of W1 at pericenter is $R_J = 88^{+52}_{-57}$ pc, which is equivalent to $3.1^{+0.8}_{-0.8}$ half-light radii. These orbit integrations suggest that, at pericenter, the Jacobi radius of W1 was within a few half-light radii of its center.

The current dynamical properties of a satellite also correspond to their infall time, as shown by Rocha et al. (2012) using subhalos from the Via Lactea II cosmological simulations. Their work found a tight correlation between orbital energy and infall time where subhalos that were accreted earlier had more time to sink into the gravitational potential of the Milky Way, resulting in energies corresponding to more tightly bound systems (see Fig. 2 of Rocha et al. 2012). Tightly bound objects cluster at small Galactocentric radii and low speeds (see Fig. 3 of Rocha et al. 2012), consistent with the properties of W1 (see Figure 10, center panel). Indeed, our orbital model for W1 suggests that W1 is one of the most tightly bound dwarf galaxies based on its total energy. From this relation, we estimate W1's infall time to be roughly 9 Gyr ago. Combining this with an orbital period of ~ 0.6 Gyr (see Figure 7, bottom panel), we can estimate that W1 has undergone ~ 15 orbits since it crossed into the virial radius of the Milky Way.

6.2. Mock tidal streams

To further probe the possibility of tidal interactions between the Milky Way and W1, we use the `gala` particle stream spray to generate simulated stellar streams for comparison with the distribution of W1 stars (Price-Whelan

804 ter distances greater than 40 kpc, indicating that the trajectory
 805 of W1 is most likely to be coming out of the Milky Way
 806 approaching apocenter.

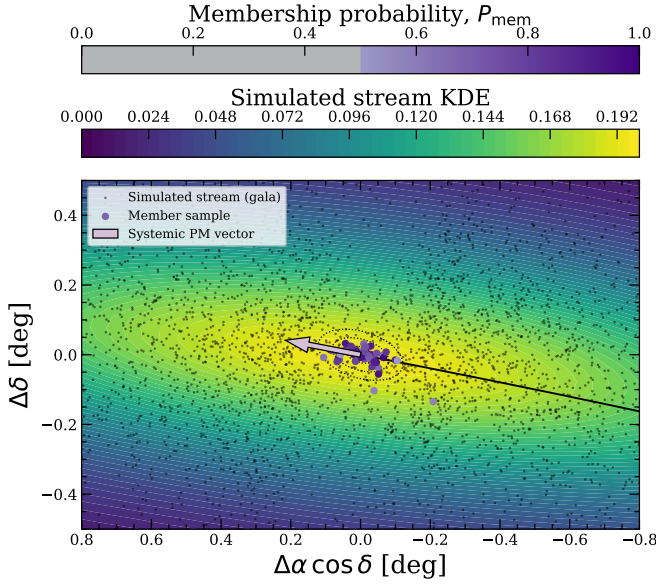


Figure 8. Spatial distribution of simulated particles from gala mock stream spray model using `MWPotential2014` of Bovy (2015) with a 50% enlarged dark matter halo ($1.2 \times 10^{12} M_\odot$). The member sample is over-plotted and color-coded according to their membership probability. The systemic proper motion vector corrected for solar reflex motion is denoted by the light purple arrow, and the three concentric dotted ellipses represent 1, 2, and $3 r_{\text{half,ell}}$.

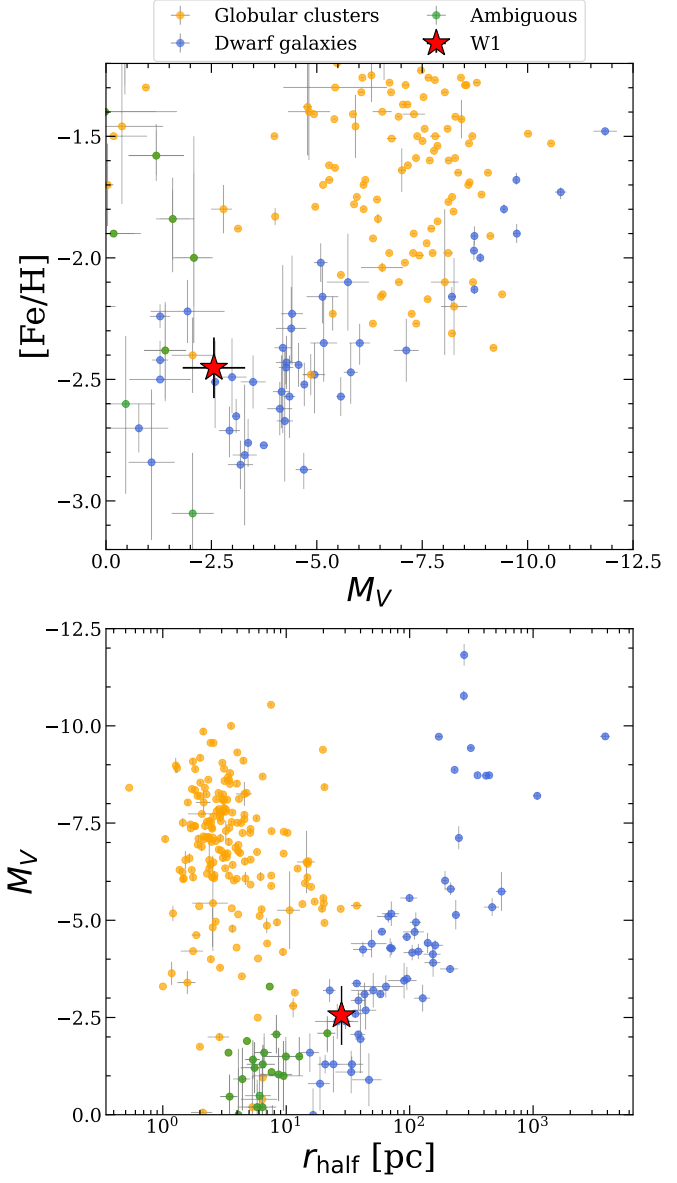


Figure 9. Comparison of W1 (red star) with other Milky Way dwarf galaxies (blue circles), globular clusters (orange circles), and ambiguous objects (green circles) taken from (Pace 2025). *Upper:* [Fe/H] iron abundance spectroscopic metallicity as a function of absolute V-band magnitude. W1 is significantly fainter compared to other dwarf galaxies in its metallicity range, which could be explained by mass loss due to tidal stripping. *Lower:* Absolute V-band magnitude vs. half-light radius. W1 is one of the faintest dwarf galaxies and has one of the smallest half-light radii.

tion, and position on the size-luminosity plane, we conclude that W1 is a dwarf galaxy.

From our kinematic analysis (§4.1), we measure a mass-to-light ratio of 660 ± 590 from the 49 non-variable member stars within $3 r_{\text{half,ell}}$. This large mass-to-light ratio, far from unity, indicates a dark matter-dominated object (e.g., Martin et al. 2007; Simon & Geha 2007). We emphasize that cut-

7. DISCUSSION

7.1. Is W1 a dwarf galaxy?

We now turn to the question of the nature of W1: is this object a dwarf galaxy or a star cluster? Due to its large mass-to-light ratio, observed metallicity spread, lack of mass segrega-

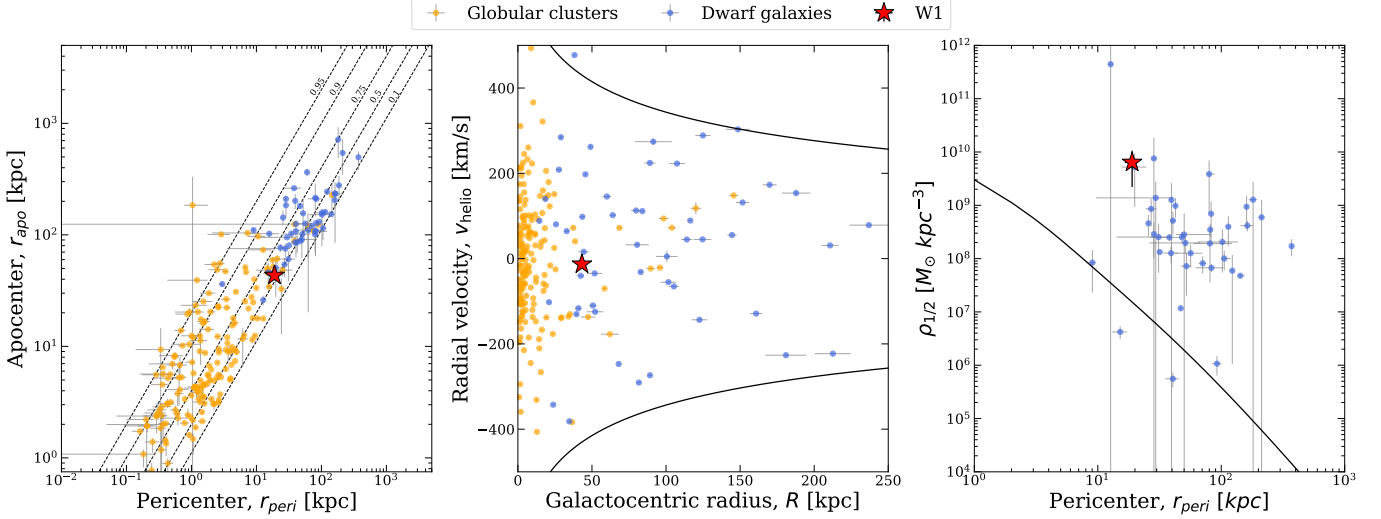


Figure 10. Comparison of the orbital properties of W1 with other Milky Way dwarf galaxies and globular clusters. W1 is denoted by a red star (see Table 2), Milky Way dwarf galaxies as blue circles, and globular clusters as orange circles (Pace 2025). *Left:* Apocenter distance as a function of pericenter distance. The locations of different orbital eccentricities are labeled as dotted lines. W1 has small pericenter and apocenter distances relative to other Milky Way dwarf galaxies. *Center:* Radial velocity as a function of Galactocentric radius, which corresponds to its binding energy and infall time (Rocha et al. 2012). The black lines represent the escape velocity curves computed using MWPotential2014 of Bovy (2015) with a 50% enlarged dark matter halo mass. W1 has one of the smallest radial speeds and Galactocentric radii, corresponding to a high binding energy and early infall time (see §6.1). *Right:* Average density within one half-light radius as a function of orbital pericenter distance. The black line shows twice the enclosed Milky Way density as a function of radius. According to Pace et al. (2022), if the satellite sits below this line, its Jacobi radius will be larger than the half-light radius and it will likely be tidal disrupting.

ting to within different half-light radii down to $2 r_{\text{half,ell}}$ does not change our results. For W1's stellar mass, its mass-to-light ratio is consistent with the larger Milky Way satellite galaxy population (Geha 2026, , Fig. 2). From our metallicity analysis (§4.2), we find evidence for a metallicity spread ($\sigma_{[\text{Fe}/\text{H}]} = 0.30^{+0.15}_{-0.11}$ dex) based on eight RGB stars with measured spectroscopic metallicities. This metallicity spread suggests that W1 has self-enriched, a property of satellites with dark matter halos that allow them to retain their gas more efficiently and go through successive epochs of star formation (e.g., Willman & Strader 2012; Kirby et al. 2013b).

We conduct a comprehensive search for the presence of mass segregation in W1 based on *HST*/ACS imaging (§5). We find a lack of mass segregation, implying a dwarf galaxy classification and consistent with previous work of Baumgardt et al. (2022). Recent simulations by Errani et al. (2025) suggest that mass segregation can occur in very low stellar mass objects, even if they host a dark matter halo. However, W1's relatively large size and luminosity compared to the objects studied prolong its relaxation time beyond a Hubble time, making this effect negligible.

Finally, we compare the structural properties of W1 to other Milky Way satellites. We rely on the Local Volume Database of Pace (2025) for a comprehensive repository of the latest literature values of the observed properties of Milky Way dwarf galaxies, globular clusters, and ambiguous objects. The position of W1 on the size-luminosity plane of

confirmed Milky Way satellites is more consistent with the the dwarf galaxy population; W1 is significantly less compact than globular clusters with similar luminosities (see Figure 9; lower panel).

7.2. Is W1 tidally disrupted?

The total mass of satellite systems are estimated under the assumption of dynamical equilibrium (Wolf et al. 2010). It is thus crucial to understand the dynamical state of W1 in order to determine whether its measured internal velocity dispersion is a true reflection of its dynamical mass. We will now weigh the evidence for and against tidal disruption.

The evidence for tidal disruption is the following. First, the spatial distribution of W1 is elongated, with an ellipticity of $\epsilon = 0.47$ (Muñoz et al. 2018b). Crucially, high-probability member stars extend out to $3 r_{\text{half,ell}}$ and are not confined to only the central regions. Although we do not see the presence of extended spatial features beyond $3 r_{\text{half,ell}}$ as suggested by previous work and we report that the number density of stars is consistent with the expected Plummer distribution, this is not inconsistent with simulations of mildly stripped satellites (e.g., Peñarrubia et al. 2009).

Second, we continue to observe an irregular velocity profile, as originally noted in Willman et al. (2011), where the velocities of stars within $\sim 0.75 r_{\text{half,ell}}$ are systematically higher (see Figure 3, upper panel). This produces a remarkably asymmetric, non-Gaussian velocity distribution (see Figure 4, lower panel). Furthermore, we find that the ve-

940 locity dispersion of the central member stars within $1 r_{\text{half,ell}}$
 941 is significantly lower than the velocity dispersion measured
 942 out to 2–4 $r_{\text{half,ell}}$, even when accounting for Milky Way in-
 943 terlopers via Gaussian mixture modeling.

944 The luminosity-metallicity relation has been shown to be
 945 tight for dwarf galaxies (Kirby et al. 2013b; Simon 2019;
 946 Geha 2026). For satellites that initially conform to this rela-
 947 tion, tidal stripping decreases their luminosity while the av-
 948 erage metallicity is unchanged. **The location of satellites to**
 949 **the left of the luminosity-metallicity relation** has been used
 950 as a diagnostic for tidal stripping (e.g., Kirby et al. 2013a,
 951 2015; Collins et al. 2020); however see Riley et al. (2026)
 952 **for a more in depth discussion.** We find evidence for this
 953 phenomenon in the case of W1 where the luminosity of W1
 954 is much fainter when compared to dwarf galaxies of similar
 955 metallicities (see Figure 9, upper panel).

956 Our **tidal-stream simulations** for a W1-like progenitor
 957 show that W1’s elongated structure is along the same axis as
 958 **the high-density regions** of the mock streams. These features
 959 are also aligned with the orbital trajectory of W1, **consistent**
 960 **with the hypothesis that tidal stripping from the Milky Way’s**
 961 **gravitational field could explain W1’s elongated and ellipti-**
 962 **cal spatial distribution.**

963 Our best-fit orbital solutions conclusively predict W1 to
 964 currently be at apocenter, with a pericentric passage $\lesssim 25$
 965 kpc. At this location, the Jacobi radius of W1 would be on
 966 the order of a few half-light radii, potentially allowing for the
 967 stripping of stars at the outskirts. We also compare the or-
 968 bital parameters of W1 with those of other Milky Way dwarf
 969 galaxies and globular clusters in Figure 10. These parame-
 970 ters were determined by following the same methods as per-
 971 formed on W1 using the MW+LMC potential (§6.1). W1
 972 has one of the smallest radial speeds and Galactocentric radii
 973 of the Milky Way’s dwarf galaxies, consistent with a system
 974 with a high binding energy and early infall time (see Figure
 975 10, center panel). In combination with its small pericenter
 976 and apocenter distances (see Figure 10, left panel), this sug-
 977 gests that slow tidal stripping from W1’s sustained passage
 978 near the Milky Way over the course of its orbit could explain
 979 W1’s elongated structural properties and irregular kinematic
 980 profile.

981 The evidence against tidal disruption is W1’s large density,
 982 which implies that its half-light radius is smaller than its Ja-
 983 cobi radius (see Figure 10, right panel). However, we note
 984 multiple other dwarf galaxies with evidence for tidal disruption
 985 also lie above this line (e.g., Boötes I, Hercules, Filion
 986 & Wyse 2021; Ou et al. 2024). If W1 is indeed tidally dis-
 987 rupted and exhibits a large density, this could suggest that
 988 tidal stripping is more efficient than previously thought.

989 Overall, we find that the evidence for tidal disruption out-
 990 weigh the evidence against it. The morphological and kine-
 991 matic properties of W1 support a scenario in which W1 is

992 experienced sustained tidal stripping due to its proximity to
 993 the Milky Way over the course of its orbit. Importantly, the
 994 presence of tidal stripping does not invalidate the evidence
 995 for W1’s classification as a dwarf galaxy. Even if its cur-
 996 rent velocity dispersion is inflated or not fully representative
 997 of its dynamical mass, we emphasize the observed metal-
 998 licity spread, lack of mass segregation, and position on the
 999 size-luminosity plane as continued evidence for W1’s dwarf
 1000 galaxy classification. Therefore, while tidal effects may com-
 1001 plicate the interpretation of the measured velocity dispersion,
 1002 we still conclude that W1 is a dwarf galaxy that is likely
 1003 tidally evolving with the Milky Way.

8. CONCLUSION

We have presented a comprehensive study of the structural,
 kinematic, chemical, and orbital properties of W1. Our main
 results are summarized as follows:

- We identify a member sample of 57 stars, including six binaries, from new and improved Keck/DEIMOS spectroscopy and *Gaia* astrometry (§2, §3.1). We measure the physical properties of W1 from the 49 of these stars out to 3 half-light radii.
- We measure a systemic velocity of $v_{\text{sys}} = -13.0^{+1.1}_{-1.1}$ km s $^{-1}$ and a velocity dispersion of $\sigma_v = 4.7^{+1.5}_{-1.3}$ km s $^{-1}$ based on a two-component Gaussian mixture model (§4.1). If W1 is in equilibrium, this implies a dynamical mass of $5.9^{+3.7}_{-3.4} \times 10^5 M_\odot$ and a mass-to-light ratio of $(M/L)_V = 660 \pm 590$.
- We measure an average metallicity of $[\text{Fe}/\text{H}] = -2.45^{+0.12}_{-0.13}$ and metallicity dispersion $\sigma_{[\text{Fe}/\text{H}]} = 0.30^{+0.15}_{-0.11}$ dex from eight member stars with CaT-based metallicity measurements (§4.2).
- We conclude that W1 is a dwarf galaxy based on its dynamical mass-to-light ratio (§4.1), observed metallicity spread (§4.2), lack of mass segregation within $\sim 1 r_{\text{half,ell}}$ (§5.2), and position on the size-luminosity plane (§7.1).
- Evidence for tidal disruption outweighs evidence against tidal disruption (§7.2). While W1 is quite dense, we find that our best-fit orbital solution (§6.1) and comparison with our simulations of tidal streams (§6.2) indicate a sustained passage near the Milky Way over the course of its orbit. This history could explain W1’s elliptical shape, asymmetric velocity distribution (§4.1), and offset on the luminosity-metallicity plane.
- We therefore caution that the internal velocity dispersion of W1 may not accurately reflect the dynamical mass of the system. The true dynamical nature of W1 may be better understood through deeper wide-field imaging and spectroscopy as well as more detailed dynamical modeling to assess the validity and use of equilibrium models.

1043 Looking ahead, the upcoming Vera C. Rubin Observatory's
 1044 Legacy Survey of Space and Time (LSST) is anticipated to
 1045 uncover a population of similarly faint, distant, and low lu-
 1046 minosity Local Group satellites. Many of these objects are
 1047 likely to resemble W1, with sparse red giant branches, un-
 1048 certain membership, and properties that blur the line between
 1049 star clusters and dwarf galaxies. **Accurate characterization**
 1050 **will require** extensive spectroscopic follow-up in order to se-
 1051 cure clean member samples, **enabling precise** kinematic and
 1052 chemical measurements. By developing the tools needed to
 1053 **study** these systems, we are better equipped to understand the
 1054 satellites LSST will reveal and their place in the broader Lo-
 1055 cal Group satellite population. From this, we can more com-
 1056 prehensively **test** the predictions of cosmological models and
 1057 **probe** the processes that govern galaxy formation, evolution,
 1058 and structure on the smallest scales.

ACKNOWLEDGEMENTS

1060 We thank the anonymous referee for their suggestions on
 1061 our manuscript that improved this work. We also thank Yas-
 1062 meen Asali and Sebastian Monzon for their insightful com-

1063 **ments. We thank Ricardo Muñoz for making his raw Mega-**
 1064 **cam photometric catalogs available.**

1065 This research has made extensive use of the Keck Ob-
 1066 servatory Archive (KOA), which is operated by the W. M.
 1067 Keck Observatory and the NASA Exoplanet Science Insti-
 1068 tute (NExSci), under contract with the National Aeronautics
 1069 and Space Administration.

1070 This work has made use of data from the European Space
 1071 Agency (ESA) mission Gaia⁶, processed by the Gaia Data
 1072 Processing and Analysis Consortium (DPAC⁷). Funding for
 1073 the DPAC has been provided by national institutions, in par-
 1074 ticular the institutions participating in the Gaia Multilateral
 1075 Agreement.

1076 **Software:** This research made use of many community-
 1077 developed or community-maintained software packages, in-
 1078 cluding (in alphabetical order): Astropy (Astropy Collabora-
 1079 tion et al. 2013), Emcee (Foreman-Mackey et al. 2013), gala
 1080 (Price-Whelan 2017), galpy (Bovy 2015), IPython (Perez
 1081 & Granger 2007), Jupyter (jupyter.org), Matplotlib (Hunter
 1082 2007), NumPy (van der Walt et al. 2011), pandas (McKin-
 1083 nney 2010), photutils (Bradley et al. 2025), SciPy (Jones et al.
 1084 2001). This research has also made use of NASA's Astro-
 1085 physics Data System.

1086 **Facility:** Gaia, Keck:II (DEIMOS)

REFERENCES

- 1087 Aliu E., et al., 2009, [ApJ](#), **697**, 1299
 1088 Armstrong B. M., Bekki K., Ludlow A. D., 2021, [MNRAS](#), **500**,
 1089 2937
 1090 Astropy Collaboration et al., 2013, [A&A](#), **558**, A33
 1091 Battaglia G., Starkenburg E., 2012, [A&A](#), **539**, A123
 1092 Baumgardt H., Faller J., Meinhold N., McGovern-Greco C., Hilker
 1093 M., 2022, [MNRAS](#), **510**, 3531
 1094 Belokurov V., et al., 2007, [ApJ](#), **654**, 897
 1095 Binney J., Tremaine S., 1987.
 1096 Bovy J., 2015, [ApJS](#), **216**, 29
 1097 Bradley L., et al., 2025, astropy/photutils: 2.2.0,
 1098 doi:[10.5281/zenodo.14889440](https://doi.org/10.5281/zenodo.14889440),
 1099 <https://doi.org/10.5281/zenodo.14889440>
 1100 Bressan A., Marigo P., Girardi L., Salasnich B., Dal Cero C.,
 1101 Rubele S., Nanni A., 2012, [MNRAS](#), **427**, 127
 1102 Bringmann T., Doro M., Fornasa M., 2009, [JCAP](#), **2009**, 016
 1103 Carrera R., Pancino E., Gallart C., del Pino A., 2013, [MNRAS](#),
 1104 434, 1681
 1105 Cerny W., et al., 2024, arXiv e-prints, p. arXiv:2410.00981
 1106 Choi J., Dotter A., Conroy C., Cantiello M., Paxton B., Johnson
 1107 B. D., 2016, [ApJ](#), **823**, 102
 1108 Collins M. L. M., Tollerud E. J., Rich R. M., Ibata R. A., Martin
 1109 N. F., Chapman S. C., Gilbert K. M., Preston J., 2020, [MNRAS](#),
 1110 491, 3496
 1111 Correa Magnus L., Vasiliev E., 2022, [MNRAS](#), **511**, 2610
 1112 D'Souza R., Bell E. F., 2022, [MNRAS](#), **512**, 739
 1113 Dey A., et al., 2019, [AJ](#), **157**, 168
 1114 Dotter A., 2016, [ApJS](#), **222**, 8
 1115 Drlica-Wagner A., et al., 2015, [ApJ](#), **813**, 109
 1116 Durbin M. J., et al., 2025, arXiv e-prints, p. arXiv:2505.18252
 1117 Erkal D., et al., 2021, [MNRAS](#), **506**, 2677
 1118 Errani R., Peñarrubia J., Walker M. G., 2025, arXiv e-prints, p.
 1119 arXiv:2505.22717
 1120 Faber S. M., et al., 2003, in Instrument Design and Performance
 1121 for Optical/Infrared Ground-based Telescopes. Edited by Iye &
 1122 Moorwood, Proceedings of the SPIE, Volume 4841, pp. 1657.
 1123 Fardal M. A., Huang S., Weinberg M. D., 2015, [MNRAS](#), **452**, 301
 1124 Filion C., Wyse R. F. G., 2021, [ApJ](#), **923**, 218
 1125 Ford H. C., et al., 1998, in Bely P. Y., Breckinridge J. B., eds,
 1126 Society of Photo-Optical Instrumentation Engineers (SPIE)
 1127 Conference Series Vol. 3356, Space Telescopes and Instruments
 1128 V. pp 234–248, doi:[10.1111/12.324464](https://doi.org/10.1111/12.324464)

⁶ <https://www.cosmos.esa.int/gaia>

⁷ <https://www.cosmos.esa.int/web/gaia/dpac/consortium>

- 1129 Foreman-Mackey D., Hogg D. W., Lang D., Goodman J., 2013,
 1130 *PASP*, **125**, 306
- 1131 Fritz T. K., Battaglia G., Pawlowski M. S., Kallivayalil N., van der
 1132 Marel R., Sohn S. T., Brook C., Besla G., 2018, *A&A*, **619**,
 1133 **A103**
- 1134 Fu S. W., et al., 2023, arXiv e-prints, p. arXiv:2306.06260
- 1135 Gaia Collaboration et al., 2023, *A&A*, **674**, A1
- 1136 Geha M., 2026, arXiv e-prints, p. arXiv:2602.10202
- 1137 Geha M., Pelliccia D., Prochaska J. X., Cerny W., Davies F. B.,
 1138 Hennawi J., Holden Dusty Reichwein B., Westfall K. B., 2026,
 1139 arXiv e-prints, p. arXiv:2602.10200
- 1140 Gullikson K., Dodson-Robinson S., Kraus A., 2014, *AJ*, **148**, 53
- 1141 Hernquist L., 1990, *ApJ*, **356**, 359
- 1142 Hinton S. R., Davis T. M., Lidman C., Glazebrook K., Lewis G. F.,
 1143 2016, *Astronomy and Computing*, **15**, 61
- 1144 Homma D., et al., 2024, *PASJ*, **76**, 733
- 1145 Hunter J. D., 2007, *Computing in Science Engineering*, 9, 90
- 1146 Husser T. O., Wende-von Berg S., Dreizler S., Homeier D., Reiners
 1147 A., Barman T., Hauschildt P. H., 2013, *A&A*, **553**, A6
- 1148 Innanen K. A., Harris W. E., Webbink R. F., 1983, *AJ*, **88**, 338
- 1149 Ji A. P., et al., 2021, *ApJ*, **921**, 32
- 1150 Jones E., Oliphant T., Peterson P., et al., 2001, SciPy: Open source
 1151 scientific tools for Python, <http://www.scipy.org/>
- 1152 Kim D., Jerjen H., Milone A. P., Mackey D., Da Costa G. S., 2015,
 1153 *ApJ*, **803**, 63
- 1154 Kirby E. N., Boylan-Kolchin M., Cohen J. G., Geha M., Bullock
 1155 J. S., Kaplinghat M., 2013a, *ApJ*, **770**, 16
- 1156 Kirby E. N., Cohen J. G., Guhathakurta P., Cheng L., Bullock J. S.,
 1157 Gallazzi A., 2013b, *ApJ*, **779**, 102
- 1158 Kirby E. N., Cohen J. G., Simon J. D., Guhathakurta P., 2015,
 1159 *ApJL*, **814**, L7
- 1160 Koposov S. E., Belokurov V., Torrealba G., Evans N. W., 2015,
 1161 *ApJ*, **805**, 130
- 1162 Li S., Liang Y.-F., Fan Y.-Z., 2021, *PhRvD*, **104**, 083037
- 1163 Loewenstein M., Kusenko A., 2010, *ApJ*, **714**, 652
- 1164 Loewenstein M., Kusenko A., 2012, *ApJ*, **751**, 82
- 1165 Longeard N., et al., 2018, *MNRAS*, **480**, 2609
- 1166 Machado R. E. G., Tauil G. C., Schweder-Souza N., 2025,
 1167 Accuracy of analytic potentials for orbits of satellites around a
 1168 Milky Way-like galaxy: comparison with *N*-body simulations
 1169 ([arXiv:2506.13813](https://arxiv.org/abs/2506.13813)), <https://arxiv.org/abs/2506.13813>
- 1170 Martin N. F., Ibata R. A., Chapman S. C., Irwin M., Lewis G. F.,
 1171 2007, *MNRAS*, **380**, 281
- 1172 Martin N. F., de Jong J. T. A., Rix H.-W., 2008, *ApJ*, **684**, 1075
- 1173 Martinez G. D., Minor Q. E., Bullock J., Kaplinghat M., Simon
 1174 J. D., Geha M., 2011, *ApJ*, **738**, 55
- 1175 Maxted P. F. L., Heber U., Marsh T. R., North R. C., 2001,
 1176 *MNRAS*, **326**, 1391
- 1177 McDaniel A., Ajello M., Karwin C. M., Di Mauro M.,
 1178 Drlica-Wagner A., Sanchez-Conde M. A., 2023, arXiv e-prints,
 1179 p. arXiv:2311.04982
- 1180 McKinney W., 2010, in van der Walt S., Millman J., eds,
 1181 Proceedings of the 9th Python in Science Conference. pp 51 – 56
- 1182 Miyamoto M., Nagai R., 1975, *PASJ*, **27**, 533
- 1183 Muñoz R. R., Côté P., Santana F. A., Geha M., Simon J. D.,
 1184 Oyarzún G. A., Stetson P. B., Djorgovski S. G., 2018a, *ApJ*, **860**,
 1185 65
- 1186 Muñoz R. R., Côté P., Santana F. A., Geha M., Simon J. D.,
 1187 Oyarzún G. A., Stetson P. B., Djorgovski S. G., 2018b, *ApJ*,
 1188 860, 66
- 1189 Navabi M., Carrera R., Noël N. E. D., Gallart C., Pancino E., De
 1190 Leo M., 2026, *MNRAS*, **546**, stag019
- 1191 Navarro J. F., Frenk C. S., White S. D. M., 1997, *The
 1192 Astrophysical Journal*, **490**, 493
- 1193 Nieto D., Mirabal N., 2010, arXiv e-prints, p. arXiv:1003.3745
- 1194 Ou X., et al., 2024, *ApJ*, **966**, 33
- 1195 Pace A. B., 2025, *The Open Journal of Astrophysics*, **8**, 142
- 1196 Pace A. B., Erkal D., Li T. S., 2022, *ApJ*, **940**, 136
- 1197 Patel E., Chatur L., Mao Y.-Y., 2024, *ApJ*, **976**, 171
- 1198 Paust N. E. Q., et al., 2009, *AJ*, **137**, 246
- 1199 Peñarrubia J., Navarro J. F., McConnachie A. W., Martin N. F.,
 1200 2009, *ApJ*, **698**, 222
- 1201 Perez F., Granger B. E., 2007, *Computing in Science Engineering*,
 1202 9, 21
- 1203 Plummer H. C., 1911, *MNRAS*, **71**, 460
- 1204 Price-Whelan A. M., 2017, *The Journal of Open Source Software*,
 1205 2
- 1206 Prochaska J. X., Hennawi J. F., Westfall K. B., Cooke R. J., Wang
 1207 F., Hsyu T., Farina E. P., 2020, arXiv e-prints, p.
 1208 arXiv:2005.06505
- 1209 Richstein H., et al., 2024, *ApJ*, **967**, 72
- 1210 Riley A. H., et al., 2026, *MNRAS*, **546**, stag029
- 1211 Rocha M., Peter A. H. G., Bullock J., 2012, *MNRAS*, **425**, 231
- 1212 Saeedi S., Sasaki M., 2020, *MNRAS*, **499**, 3111
- 1213 Schiavon R. P., Barbry B., Rossi S. C. F., Milone A., 1997, *ApJ*,
 1214 479, 902
- 1215 Schlegel D. J., Finkbeiner D. P., Davis M., 1998, *ApJ*, **500**, 525
- 1216 Siegel M. H., Shetrone M. D., Irwin M., 2008, *AJ*, **135**, 2084
- 1217 Simon J. D., 2018, *ApJ*, **863**, 89
- 1218 Simon J. D., 2019, *ARA&A*, **57**, 375
- 1219 Simon J. D., Geha M., 2007, *ApJ*, **670**, 313
- 1220 Sirianni M., et al., 2005, *PASP*, **117**, 1049
- 1221 Smith S. E. T., et al., 2024, *ApJ*, **961**, 92
- 1222 Sohn S. T., et al., 2007, *ApJ*, **663**, 960
- 1223 Stetson P. B., 1987, *PASP*, **99**, 191
- 1224 Stetson P. B., 1992, in Worrall D. M., Biemesderfer C., Barnes J.,
 1225 eds, Astronomical Society of the Pacific Conference Series Vol.
 1226 25, Astronomical Data Analysis Software and Systems I. p. 297

- 1227 Torrealba G., et al., 2016, [MNRAS](#), **463**, 712
1228 Tripathi A., Panwar N., Sharma S., Kumar B., Rastogi S., 2023,
1229 [Journal of Astrophysics and Astronomy](#), **44**, 61
1230 Walker M. G., Mateo M., Olszewski E. W., Bernstein R., Wang X.,
1231 Woodroofe M., 2006, [AJ](#), **131**, 2114
1232 Weatherford N. C., Chatterjee S., Kremer K., Rasio F. A., 2020,
1233 [ApJ](#), **898**, 162
1234 Willman B., Strader J., 2012, [AJ](#), **144**, 76
1235 Willman B., et al., 2005, [AJ](#), **129**, 2692
1236 Willman B., et al., 2006, [arXiv e-prints](#), pp astro-ph/0603486
1237 Willman B., Geha M., Strader J., Strigari L. E., Simon J. D., Kirby
1238 E., Ho N., Warrens A., 2011, [AJ](#), **142**, 128
1239 Wolf J., Martinez G. D., Bullock J. S., Kaplinghat M., Geha M.,
1240 Muñoz R. R., Simon J. D., Avedo F. F., 2010, [MNRAS](#), **406**,
1241 1220
1242 van der Marel R. P., Kallivayalil N., 2014, [ApJ](#), **781**, 121
1243 van der Walt S., Colbert S. C., Varoquaux G., 2011, [Computing in
1244 Science Engineering](#), **13**, 22

1245

APPENDIX

1246 A. DETAILS OF STARS USED IN OUR ANALYSIS

1247 Table A3 present the properties of the 73 stars used in our
 1248 analysis, including the 57 stars in our member sample (§3.2;
 1249 $P_{\text{mem}} > 0.5$) and the 65 stars used in our mixture model (§4.1;

1250 $P_{\text{mem,nov}} > 0.1$, $r_{\text{half,ell}} < 3$, Var $\neq 1$). We refer the reader
 1251 to Geha et al. (2026) for a detailed discussion of the data
 1252 reduction. The full table of stars, including non-members, is
 1253 available in Table A3 of Geha et al. (2026).

Table A3. Measured properties of Keck/DEIMOS stars used in our analysis.

RA	DEC	v	v_{err}	r_o	r_{err}	g_o	g_{err}	[Fe/H]	[Fe/H] _{err}	gaia_source_id	Var	P_{mem}	Sample
[deg]	[deg]	[km/s]	[km/s]	[mag]	[mag]	[mag]	[mag]	–	dex	–	–	–	–
162.011806	50.915625	-21.38	1.10	16.067	0.020	16.721	0.020	-1.34	0.18	–	–	0.57	1
162.468917	51.061806	-19.51	0.69	18.045	0.020	18.632	0.020	-2.56	0.13	835977180433181056	0	0.68	1
162.325208	51.038000	-6.49	0.80	18.057	0.020	18.637	0.020	-2.31	0.13	8359771820314006528	1	0.75	1
162.282500	50.947306	-11.87	1.37	18.294	0.020	18.218	0.020	–	–	835970136686823040	–	0.58	1
162.304708	51.042306	-24.46	3.03	19.790	0.020	19.429	0.020	–	–	836722438863176448	1	0.66	1
162.322625	51.057194	-11.87	1.16	19.997	0.020	20.445	0.020	-2.60	0.19	836722473222915968	0	0.81	1
162.366083	51.062861	-13.42	1.82	20.282	0.020	20.693	0.020	-2.62	0.22	835977725893619712	0	0.78	1
162.175708	51.033611	-6.48	1.33	20.364	0.020	20.595	0.020	–	–	836722889836066048	1	0.50	1
162.283708	51.040833	-9.97	0.97	20.429	0.020	20.905	0.020	-1.79	0.18	836722335783961216	0	0.90	1
162.292208	51.050083	-11.46	1.29	20.434	0.020	20.851	0.020	-2.72	0.19	836722404504886912	0	0.79	1
162.316583	51.040694	-9.50	2.24	20.471	0.021	20.925	0.020	-2.36	0.24	8359771816018616320	0	0.62	1
162.338167	51.058389	-12.89	1.80	20.750	0.021	21.120	0.021	-2.85	0.30	8359771854673199616	0	0.70	1
162.394000	51.044389	-64.30	1.96	20.766	0.021	21.224	0.021	–	–	835977416655970816	0	0.00	0
162.242208	51.048306	-6.74	1.77	20.795	0.021	21.321	0.022	–	–	836722198345008512	0	0.62	1
162.420125	51.061194	-15.91	1.75	20.891	0.025	21.198	0.023	–	–	835977588454665856	0	0.90	1
162.379000	51.061389	-15.15	2.88	20.903	0.021	21.227	0.021	–	–	835977691533881088	0	0.94	1
162.319833	51.067667	-17.51	2.14	20.915	0.021	21.276	0.021	–	–	836722546237412608	0	0.92	1
162.403417	51.064250	-10.79	3.05	20.998	0.021	21.216	0.021	–	–	835977588454666368	0	0.80	1
162.512042	51.042278	-13.00	2.47	21.184	0.021	21.598	0.021	–	–	–	0	0.62	1
162.379208	51.026111	-73.13	2.79	21.270	0.021	21.699	0.021	–	–	–	–	0.00	0
162.242000	51.089500	-98.13	3.04	21.330	0.024	21.859	0.029	–	–	–	0	0.00	0
162.366917	51.058194	-8.43	6.41	21.356	0.021	21.544	0.021	–	–	–	0	0.91	1
162.238083	51.042056	-12.68	3.64	21.395	0.022	21.631	0.021	–	–	–	0	1.00	1
162.366917	51.031000	-23.41	5.63	21.405	0.022	21.613	0.021	–	–	–	0	0.78	1
162.359708	51.054556	-8.05	2.75	21.425	0.022	21.654	0.021	–	–	–	0	0.95	1
162.302292	51.051500	-6.03	4.13	21.438	0.022	21.679	0.021	–	–	–	0	0.89	1
162.464708	51.031194	-21.26	2.85	21.482	0.022	21.866	0.021	–	–	–	0	0.46	0
162.354417	51.047889	0.50	3.96	21.484	0.021	21.729	0.021	–	–	–	0	0.64	1
162.281917	51.029500	-8.58	5.55	21.505	0.022	21.732	0.021	–	–	–	0	0.91	1
162.394917	51.074583	-18.42	4.47	21.512	0.022	21.798	0.021	–	–	–	0	0.79	1
162.185083	51.035028	-8.09	3.40	21.521	0.022	21.770	0.021	–	–	–	1	0.90	1
162.264208	51.013500	-3.26	7.06	21.544	0.022	21.649	0.021	–	–	–	–	0.66	1
162.373917	51.049500	-19.65	4.41	21.586	0.022	21.784	0.021	–	–	–	0	0.88	1
162.291417	51.015611	-6.23	6.02	21.625	0.022	21.820	0.021	–	–	–	0	0.83	1
162.296750	51.075083	-9.78	3.27	21.638	0.022	21.865	0.021	–	–	–	0	0.91	1
162.447375	51.059639	-7.81	6.17	21.658	0.022	21.933	0.021	–	–	–	0	0.84	1

Table A3 continued

Table A3 (continued)

RA	DEC	v	v_{err}	r_o	r_{err}	g_o	g_{err}	[Fe/H]	[Fe/H] _{err}	gaia_source_id	Var	P_{mem}	Sample
[deg]	[deg]	[km/s]	[km/s]	[mag]	[mag]	[mag]	[mag]	–	dex	–	–	–	–
162.365208	51.059111	-11.66	4.76	21.676	0.022	21.901	0.021	–	–	–	0	0.98	1
162.354333	51.040333	-14.41	4.94	21.702	0.022	21.932	0.021	–	–	–	0	0.98	1
162.325250	51.054694	-3.68	10.09	21.715	0.023	21.842	0.021	–	–	–	–	0.75	1
162.203083	51.054694	63.33	5.23	21.751	0.022	22.223	0.022	–	–	–	–	0.00	0
162.271500	51.028389	-9.53	4.68	21.771	0.023	21.941	0.021	–	–	–	–	0.93	1
162.340083	51.045917	-8.79	6.32	21.798	0.023	22.021	0.022	–	–	–	1	0.90	1
162.323292	51.045389	-18.42	5.28	21.818	0.023	22.046	0.022	–	–	–	0	0.90	1
162.412500	51.082611	-11.91	11.86	21.832	0.023	22.095	0.023	–	–	–	–	0.93	1
162.321028	51.072971	-21.50	13.57	21.916	0.023	22.209	0.022	–	–	–	–	0.73	1
162.339500	51.042889	-6.48	10.91	22.000	0.023	22.209	0.022	–	–	–	–	0.94	1
162.307500	51.006306	24.23	7.34	22.090	0.023	22.368	0.022	–	–	–	–	0.07	0
162.316875	51.049889	-13.64	7.03	22.110	0.024	22.314	0.022	–	–	–	–	0.99	1
162.362833	51.058361	-9.94	14.21	22.118	0.024	22.334	0.023	–	–	–	–	0.98	1
162.348625	51.051083	7.51	4.74	22.141	0.024	22.407	0.023	–	–	–	–	0.38	0
162.315500	51.022611	-29.34	5.03	22.142	0.024	22.478	0.023	–	–	–	–	0.41	0
162.261708	50.994500	-13.21	11.12	22.164	0.024	22.416	0.023	–	–	–	–	0.95	1
162.450625	51.030111	-15.70	5.60	22.250	0.025	22.566	0.023	–	–	–	–	0.81	1
162.481266	51.063726	-7.74	5.97	22.271	0.025	22.540	0.024	–	–	–	–	0.85	1
162.312208	51.048306	-0.75	5.33	22.355	0.026	22.610	0.024	–	–	–	0	0.73	1
162.191875	51.000000	-56.49	14.64	22.364	0.025	22.625	0.023	–	–	–	–	0.10	0
162.328792	51.081500	-28.43	13.10	22.430	0.026	22.656	0.024	–	–	–	–	0.68	1
162.306000	51.045389	-2.56	6.82	22.446	0.026	22.751	0.024	–	–	–	0	0.71	1
162.386417	51.074194	-17.77	7.54	22.448	0.026	22.757	0.024	–	–	–	–	0.83	1
162.440208	51.035806	-23.59	6.94	22.501	0.027	22.811	0.024	–	–	–	–	0.74	1
162.448375	51.034389	-16.27	10.24	22.555	0.028	22.848	0.025	–	–	–	–	0.90	1
162.295375	51.037194	-26.38	12.14	22.591	0.028	22.878	0.025	–	–	–	–	0.74	1
162.364917	51.033611	-32.65	6.73	22.615	0.028	22.855	0.025	–	–	–	0	0.45	0
162.341583	51.055000	-37.80	13.69	22.640	0.028	22.957	0.025	–	–	–	0	0.42	0
162.292417	51.082694	50.93	10.37	22.752	0.028	23.268	0.029	–	–	–	–	0.00	0
162.434917	51.050694	-28.43	2.07	22.774	0.030	22.994	0.026	–	–	–	–	0.52	1
162.281203	51.055597	8.72	8.25	22.793	0.031	23.199	0.027	–	–	–	–	0.29	0
162.373000	51.062611	82.11	8.87	22.829	0.032	23.124	0.028	–	–	–	–	0.00	0
162.269708	51.054611	-23.40	6.03	22.836	0.031	23.088	0.026	–	–	–	1	0.76	1
162.326000	51.059500	-24.76	9.18	22.858	0.031	23.114	0.027	–	–	–	–	0.76	1
162.227000	51.057889	-22.41	9.30	23.014	0.034	23.308	0.030	–	–	–	–	0.84	1
162.496000	51.048806	32.14	6.15	23.028	0.034	23.339	0.030	–	–	–	–	0.02	0
162.216547	51.040881	29.80	8.04	23.233	0.042	23.659	0.035	–	–	–	–	0.03	0